

## Answers to David R. Thompson (Referee 1)

### General comments

The authors provide a well-motivated study into the small-scale vertical and horizontal structure of cloud thermodynamic phase. The experiment is impressive in scope, including both passive (horizontal mapping) and active (vertical) airborne instruments, combined with additional large eddy simulations of vertical structure. The authors conclude that, given their data, "the cloud top small-scale horizontal variability reacts to changes in the vertical distribution of the cloud thermodynamic phase." This is an important topic for GCM parameterization. The manuscript is very clear and well-written, though I have identified some potential weaknesses in both the methodology and scope that the authors might consider. Overall: I am sympathetic to, and appreciative of, the authors' attention to fine-scale thermodynamic phase. However, such measurements may eventually require a more quantitative and comprehensive account for other potential confounding variance at scales of 100m or less. Taking this on would significantly improve the paper.

We thank the reviewer for his careful reading of the manuscript and his suggestions. With our reply and the revised version of our manuscript, we hope to address all the comments in a satisfying way. Our answers are structured and indicated as follows: reviewer comments (bold), answers, changes in the manuscript (italic).

1. **2D photon transport effects in the cold outbreak case.** As far as I can tell from the description, the authors' phase index retrieval method assumes RTMs of a homogeneous plane-parallel cloud surface; this is fine, except that they then apply that to interpret a heterogeneous cloud body where there is likely to be considerable horizontal photon transport due to scattering within the cloud itself. Horizontal transport implies the retrieval has a locale-specific geometric sensitivity "footprint" which I suspect is larger than the 10m spatial resolution of AISA. But the authors' maps seem to interpret every pixel at native resolution as if it were an effective discriminator of cloud phase at that location - hence the frequency distribution histograms of Fig. 5. Additionally, the exposure to incident sunlight and slant path through the cloud might vary since the cloud thickness and altitude are also varying on similar scales (i.e. "Domes" and "Holes" but also even finer-scale structure in the retrievals). While a full 3D simulation may be overkill, the authors would ideally find sufficient account for the cloud horizontal heterogeneity in their algorithm to avoid hallucinating compositional features which might, for example, be artifacts of selfshading effects or other horizontal heterogeneity. As a thought experiment, imagine where a reasonable estimate of horizontal sensitivity could be determined and the AISA data were convolved with a sensitivity kernel before applying the retrieval. If this caused the LWP retrieval to look more like the 100+ m rows of Figs. 10 and 11, how would it affect the authors' top-level claims and interpretations of fine-scale structure?

We agree with the reviewer that the aspects related to 3D cloud geometry and 3D radiative transfer were not adequately addressed in the original manuscript. In the revised manuscript, we added two exercises to justify the interpretation of the AISA Hawk data. In order to account for the horizontal photon transport occurring in the considered case studies, a convolution kernel was derived by comparing 3D radiative transfer simulations performed with the Monte Carlo Atmospheric Radiative Transfer Simulator (MCAraTS, Wang et al., 2012) with 1D radiative transfer simulations performed with the Library for Radiative transfer (libRadtran) code (Mayer and Kylling, 2005; Emde et al., 2016). A narrow stripe of pure-ice was embedded in a pure liquid stratiform cloud, causing a recognizable narrow peak in the reflected cloud top radiance. The cross-correlation between the simulated 1D and 3D radiance for different

sun-sensor geometries (i.e. different solar azimuth angles and different viewing angles) was used to determine the convolution kernel. The AISA Hawk measurements were deconvolved using the Richardson-Lucy deconvolution algorithm (Richardson, 1972; Lucy, 1974), similarly to Zinner et al. (2006). The cloud top properties ( $R_{1240}$ ,  $\mathcal{I}_s$ ,  $\tau$ ,  $r_{\text{eff}}$ , and  $LWP$ ) were recalculated based on the deconvolved radiance fields.

Once the radiance fields are deconvolved, the observed small-scale features on the cloud top become more apparent. Regions of low reflected radiance present lower values and viceversa for areas with high radiance. For the presented case studies, this causes the relationship between  $R_{1240}$  and  $\mathcal{I}_s$  to spread over a slightly larger range of values than originally, but it maintains its general behavior, with  $R_{1240}$  and  $\mathcal{I}_s$  increasing simultaneously on 25 May and presenting opposite trends on 2 June. In the same way, the retrieved  $LWP$  keeps its features: on 25 May it increases towards optically thicker areas, indicating the natural variability of liquid water top layer. On the contrary, on 2 June it presents anomalously high values, specially in areas of low reflectivity, which results from neglecting the ice in the retrieval of  $\tau$  and  $r_{\text{eff}}$ , as the reviewer as well notes in comment 2. As the deconvolution did not change the general features of  $R_{1240}$ ,  $\mathcal{I}_s$ , and the retrieved  $LWP$ , the conclusions drawn in the original manuscript still hold.

The convolution kernel applies only for horizontal photon transport, but does not account for shadows in the AISA Hawk fields. In a second exercise, we estimated the effect of the 3D cloud structure on the retrieved cloud top properties. The correction of self-shading artifacts would require highly spatially resolved information of the cloud top geometry. Although AMALi (lidar) provides the cloud top height of the nadir cloud section, its 1 s sampling rate does not allow a thorough reconstruction of the cloud top structures. Additionally, no information about the cloud regions out of nadir is available. Therefore, the correction of the radiance fields from self-shading artifacts is not possible. However, 3D radiative transfer simulations allow to interpret the effects that shading artifacts and an inhomogenous spatial distribution of the thermodynamic phase have on the cloud top properties  $R_{1240}$ ,  $\mathcal{I}_s$ , and  $LWP$ . These effects were analyzed using idealized 3D radiative transfer simulations. It has been found that, although shaded regions may present an increment in  $\mathcal{I}_s$  related to a lower  $R_{1240}$ , an associated anomalously increase in the retrieved  $LWP$  is not observed in the simulations. However, simulations with an inhomogeneous distribution of cloud phase result in an increase of the retrieved  $LWP$ . This increase results from assuming pure liquid water clouds in the  $LWP$  retrieval procedure. Therefore, the observations of 2 June can be explained by the distribution of ice and liquid water, but are not significantly effected by shades.

#### Changes:

- A new Appendix A, including detailed explanation of the procedure to derive the convolution kernel and results of 3D simulations to analyze the effects of shades and phase inhomogeneities, was included.
- p4 113: “*At this resolution, horizontal photon transport needs to be taken into account. The AISA Hawk measurements have been corrected from this effect using the deconvolution algorithm introduced in App. A*” was included.
- p6 112: “*Appendix A analyzes the different impact of shades and inhomogeneous thermodynamic phase distributions in the retrieved LWP*” was included.
- Tables 1 and 2 were updated.
- Figures 4, 5, 6, 7, 8, 9, 10, and 11 were updated.
- Figures 4 and 6 present now a narrower swath than before because artifacts resulting from the deconvolution procedure were removed. For the same reason, in the resolution analysis in Sect. 5 the pixel sizes were adapted to the new available data (instead of 25 m, 100 m, 500 m, and 1000 m pixel sizes, 30 m, 90 m, 450 m, and 900 m have been considered).

2. **Accuracy of the slope phase index for characterizing mixed phase clouds.** While  $\mathcal{I}_s$  has been demonstrated as an effective way to discriminate pure clouds, it is not always clear how to interpret  $\mathcal{I}_s$  for mixed phase clouds since, as the authors note, the vertical partitioning can favor one or the other. In fact, the particles can themselves be mixed together at *very* small spatial scales - such intimate mixing could contribute to the strong overestimation of *LWP* for the warm air advection scenario (as noted at the bottom of page 11). Even the interpretation as intimately-mixed particles is suspect though since the "fishnet" manifold is so tight near the AISA data in Fig. 8. Does the ratio really provide enough measurement power to discriminate mixed phases, particularly given the uncharacterized uncertainties I mention above - how can we exclude self-shading and sky view fractions as an alternative account for the apparent difference between "Holes" and "Domes?"

We agree with the reviewer about the limited capabilities of  $\mathcal{I}_s$  alone to identify mixed-phase cases, as we explain in Sect. 6 (p22 117-20). A typical photon penetration depth inferior to 200 m in the wavelength range defining  $\mathcal{I}_s$  (Ehrlich et al., 2009) prevents its sensitivity to phase inhomogeneities occurring in low cloud layers, as it is the case for 25 May. Nevertheless, in this case, the misclassification of the scene as pure liquid produces no further artifacts on the retrieved cloud properties, which also relate to the pure liquid layer top and yield a value of the retrieved *LWP* comparable to that based on the 89 GHz channel of MiRAC. The correct classification of these stratified distributions of cloud phase as mixed-phase based on  $\mathcal{I}_s$  is only possible if information on the cloud vertical structure, e.g. provided by active remote sensing, is available.

The  $\mathcal{I}_s$  on 2 June presents two clear differences compared to the one on 25 May: it increases its value in areas of low  $R_{1240}$  and the values cannot be reproduced by simulations of pure liquid water clouds (Fig. 7). Additionally, the *LWP* retrieved based on the AISA Hawk radiance is on average higher than the retrieval of MiRAC and acquires specially high values in areas of low  $R_{1240}$  (Fig. 6i). 3D radiative transfer simulations included in the new App. A show that, although shaded areas in the image may produce an increment in  $\mathcal{I}_s$ , they cannot account for the high values of *LWP* if no increase of the ice concentration is present. Therefore, it is only the combination of  $R_{1240}$ ,  $\mathcal{I}_s$ , and the retrieved *LWP* that allows the identification of mixed-phase scenes. Even after combining the information provided by these three quantities, Fig. 8 highlights that the mixed-phase identification is only possible if the ice phase appears directly at cloud top.

The classification between "domes" and "holes", based on the 25th percentile of  $R_{1240}$  and the 75th percentile of  $\mathcal{I}_s$ , isolates the small-scale features observed on the cloud top geometry (the "holes" correspond to the overlaid contours of Figs. 6a and 6c). Although it is not possible to assure that the holes are not influenced by shadows, their enhanced *LWP* with respect to the "domes" regions (Fig. 6i) supports our hypothesis of mixed-phase over shades effects, similar to the simulations in App. A. The comparison of the measurement, classified in holes and domes, with the mixed-phase scenarios presented in Figs. 8b and 8c highlights that the different  $R_{1240}$  and  $\mathcal{I}_s$  observed in the cloud holes compared to the cloud domes can be due to several reasons. According to these two mixing-scenarios, the high values of  $\mathcal{I}_s$  in areas of low  $R_{1240}$  are due to either larger ice fractions or larger particle sizes. However, as we mention on p16 13-7, the large possibilities to combine *IWP*, *LWP*,  $r_{\text{eff,ice}}$ , and  $r_{\text{eff,liquid}}$  as input to the radiative transfer simulations, make it impossible to find the perfect mixing scenario that fits the observations completely and to conclude which mixing scenario was more likely to happen. Using more realistic vertical profiles of *LWC*, *IWC*,  $r_{\text{eff,ice}}$ , and  $r_{\text{eff,liquid}}$  provided by the LES simulations can shed light over this issue.

Changes:

- p22 117 was updated to "*The comparison of both cloud cases highlights the limitations of passive remote sensing alone to identify layered mixed-phase structures if the ice is not sufficiently close to the*

cloud top. In particular in these cases, the combination of active and passive remote sensing is crucial to fully characterize the horizontal and vertical distribution of ice and liquid particles in mixed-phase clouds.”

3. **Formal hypothesis testing, or uncertainty quantification or propagation.** The general character of the manuscript is to bring together multiple measurement modes (*LWP* by AISA and MiRAC) and conclude that both are important to interpret diverse cloud structure. Fair enough, but do the authors have an uncertainty budget for either instrument? For example, what is the error in the Backscatter - the vertical profiles seem very qualitative in nature and it is unclear to what degree the temporal axis represents meaningful change in structure. This is important in comparing said structure to the *LWP* maps - which are themselves uncertain up to a level determined by the instrument noise and unknowns in the observation system. LES analysis is of a similarly qualitative nature, and an important first step which is meritorious as an exercise, but given the large mismatch between distributions of simulated and measured  $\mathcal{I}_s$  it is not clear that the LES has successfully explained or even accounts for the observations. Can the authors formulate this as a formal hypothesis test of some kind?

(a) *Uncertainty*

The uncertainty of the AISA Hawk radiance fields is a combination of the calibration uncertainty and noise in the measured signal and has been estimated to be in the range of 6% (Schäfer et al., 2013). Error propagation allows the estimation of the uncertainty in the cloud top properties and eventually yields a *LWP* between  $2.0 \text{ g m}^{-2}$  and  $36 \text{ g m}^{-2}$  with a 36% uncertainty for case on 25 May and a *LWP* between  $166 \text{ g m}^{-2}$  and  $380 \text{ g m}^{-2}$  with a 32% uncertainty for the case on 2 June.

The uncertainty of the *LWP* retrieval based on measurements of the 89 GHz passive channel of MiRAC is addressed in App. B (former App. A). The major source of uncertainty results from the determination of the clear sky brightness temperature, TB0. The two considered cases have an estimated uncertainty in the range of 5% to 6% ( $5 \text{ g m}^{-2}$  for  $100 \text{ g m}^{-2}$  *LWP* and  $12 \text{ g m}^{-2}$  for  $200 \text{ g m}^{-2}$  *LWP*). Therefore, the MiRAC *LWP* on 25 May ranges between  $20 \pm 1 \text{ g m}^{-2}$  and  $40 \pm 2 \text{ g m}^{-2}$ , in agreement with the retrieval of AISA Hawk for the thicker cloud regions. On 2 June, the MiRAC *LWP* ranges between  $90 \pm 5 \text{ g m}^{-2}$  and  $120 \pm 7 \text{ g m}^{-2}$ , presenting lower values than the AISA Hawk *LWP*.

The radar reflectivity of MiRAC, shown in Fig. 3, has an uncertainty of 0.5 dB (Mech et al., 2019). The lidar backscatter of AMALi is defined as in Langenbach et al. (2019). Its uncertainty is calculated using a maximum-error propagation which takes into account signal-inherent error sources, like noise, and uncertainties from assumptions in the retrieval. However, in this study, the lidar backscatter signal is interpreted only qualitatively to determine the cloud top altitude and the upper-most cloud structure relative to increments in the radar signal, hinting the existence and thickness of the liquid top layer. The geometry of the backscatter signal was corrected using the aircraft GPS and INS data. The magnitude of the lidar backscatter signal is used only to differentiate clean air from cloudy regions, with Fig. 3 displaying only the latest. A backscatter ratio of 20 (i.e.  $\log(\text{BSC}532) = 3$ ) is 20 times larger than the signal of clear air and was chosen as threshold to discriminate the cloud signal from any (much lower) aerosol signal (Gutleben et al., 2019).

Changes:

- p4 l11: “Considering uncertainties due to the calibration procedure and noise in the measured signal, the uncertainty in the radiance is estimated to be in the range of 6% (Schäfer et al., 2013)” was included.

- p8 14: “The combination of measurements is interpreted qualitatively to gain an insight into the clouds vertical structure” was included.
- p8 15: “defined as in Langenbach et al. (2019)” was included.
- p8 125 was updated to “Mean values and associated uncertainty of the cloud properties are summarized in Tab. 1”.
- p11 14 was updated to “Table 1 presents the mean values and associated uncertainty the presented cloud properties”.
- The uncertainty of the cloud top properties was included in Tab. 1 and its caption was updated to “Average value and uncertainty ( $\Delta$ ) of the cloud top properties derived from the measurements of AISA Hawk on 25 May and on 2 June. Independent estimations of the LWP range by the passive 89 GHz channel of MiRAC are also included.”

(b) *Large Eddy Simulations*

It is true that ICON-LEM did not fully reproduce the observations. ICON-LEM is a relatively new model and its performance in Arctic conditions is not yet completely evaluated (Schemann and Ebell, 2020). However, based on the comparisons with the observations, we tried to identify which aspects of the model did lead to the observed discrepancies, e.g. low ice crystal concentration. Therefore, for 25 May, the ICON-LEM produced  $LWC$  and  $IWC$  profiles (Fig. 9a) are in general in agreement with the active remote sensing in Fig. 3a (i.e. mainly liquid at cloud top from which ice precipitates). The associated  $R_{1240}$  and  $\mathcal{I}_s$  reproduce the AISA Hawk measurements on that day, being mainly affected by the higher concentration of liquid water at cloud top and presenting typical values corresponding to liquid water clouds. The knowledge of the cloud vertical structure provided by ICON-LEM allows manipulating the fields with the purpose of understanding how the cloud  $R_{1240}$  and  $\mathcal{I}_s$  react under different theoretical scenarios. In this way, an additional test case where the ICON-LEM  $IWC$  was doubled was included. Even with this anomalously increased ice concentration,  $R_{1240}$  and  $\mathcal{I}_s$  keep being influenced mainly by the liquid top layer.

On 2 June, the original ICON-LEM  $IWC$  is negligible. Hence, the associated  $R_{1240}$  and  $\mathcal{I}_s$  agree with simulations corresponding to liquid water clouds, but do not reproduce the AISA Hawk measurements on that day. Artificially enhancing 1000 times the  $IWC$  provided by ICON-LEM in order to obtain values in the same order of magnitude than the  $LWC$ , reveals its proximity to the cloud top and originates an observable impact on  $R_{1240}$  and  $\mathcal{I}_s$ . Their values spread towards the pure ice region and now reproduce the AISA Hawk observations. The reasons why ICON-LEM appears to produce so little ice on this day are unclear. Nevertheless, combining LES with radiative transfer simulations and its comparison to spectral measurements has the potential to identify misperformances of ICON-LEM, which can be used to improve its internal parameterizations.

When comparing ICON-LEM and observations, the setup of this comparison needs to be considered carefully. The larger spread of the ICON-LEM data in the  $R_{1240}$  -  $\mathcal{I}_s$  diagram compared to the measurements of AISA Hawk is due to the larger spatial area considered in the LES (Fig. 2). In this larger region, the LES cloud field has a higher variability than the limited narrow line of the measurements, e.g. the ICON-LEM domain features cloud holes which are not overflowed by AISA Hawk. We selected this larger domain of ICON-LEM in order to obtain a statistically robust number of grid points.

Changes:

- The description of ICON-LEM and its setup was moved to the new subsection *2.3 Large Eddy Simulations (LES)*. At the beginning, we state: “Simulations using the ICOSahedral Non-hydrostatic atmosphere model (ICON), operated in its Large Eddy Model (LEM) configuration (Heinze et al.,

2017; Dipankar et al., 2015) provide a quantitative view into the cloud vertical structure. The simulated cloud vertical profiles were used as input for radiative transfer simulations to analyze the impact of different vertical distributions of the cloud phase on the cloud top horizontal variability”.

- Section 4 was shortened and renamed to *Comparison of measurements and LES*. Its beginning was updated to “Comparing simulated cloud reflectivities and phase index based on ICON-LEM cloud fields with the measurements of AISA Hawk will help to evaluate the conclusions about the vertical structure of the cloud thermodynamic phase drawn in the previous section”.

- p18 l3: “located outside the measurement area of AISA Hawk” was included.

- p18 l18: “which were not observed by AISA Hawk” was changed to “which were located outside the AISA Hawk measurement region”.

#### **Minor technical clarification:**

##### **How do the horizontal (i.e.) spatial scales compare between Fig. 3 and the AISA data?**

The temporal axis of Figs. 3a and 3b coincides with the temporal axis of Figs. 4 and 6, respectively. Therefore, the measurements in Figs 3a and 3b cover the same distance in flight direction than Figs. 4 and 6 (i.e. 4.7 km on 25 May and 5.6 km on 2 June). With a sampling frequency of 1 s and 1.3 s respectively, AMALi and MiRAC have a spatial resolution of 80 m and  $\sim 100$  m on 25 May ( $80 \text{ m s}^{-1}$  flight speed) and 90 m and  $\sim 120$  m on 2 June ( $90 \text{ m s}^{-1}$  flight speed).

##### Changes:

- Spatial axes were included in Fig. 3.

## Answers to Anonymous Referee #2

### General comments

**This paper uses a combination of active and passive remote sensing instrumentation to characterize the small scale structure of cloud thermodynamic phase using two case studies observed in the Arctic. The paper is well written, gives significant results and the approach seems technically sound. Thus, as such, I think it is appropriate for publication in ACP. However, there are a few minor editorial comments and some additional points that the authors might want to consider before the publication is finalized.**

We thank the reviewer for her/his careful reading of the manuscript and her/his suggestions. With our reply and the revised version of the manuscript, we hope to address all the comments in a satisfying way. Our answers are structured and indicated as follows: reviewer comments (bold), answers, changes in the manuscript (italic).

**I would like to see more explanation on why the two particular case studies were chosen and how representative these case studies are of conditions encountered in the Arctic in general. Although cases of single-layer mixed-phase clouds do occur in the Arctic as the authors state, and although they are nice to examine from a process oriented perspective because it involves the complications of interactions between different cloud layers, past studies have suggested that multi-layer clouds and even multilayer mixed-phase clouds may be more common than these single-layer clouds. Thus, some explanation of how the results from these special cases are applicable in general to remote sensing (especially cases when active remote sensing data are not available) would be appropriate.**

The two cloud cases were chosen because they represent two contrasting cases of Arctic single-layer boundary-layer clouds (i.e., warm air advection vs. cold air outbreak), providing different conditions for cloud remote sensing. Even when categorized into warm air advection and cold air outbreak, we do not intend to draw general conclusions about the cloud properties of these scenarios. This could only be done on statistical basis, analyzing more cloud cases.

As we showed in the manuscript, the interpretation of passive remote sensing is already challenging for single-layer mixed-phase clouds. Therefore, the study focused on this specific type of Arctic clouds and excluded cases of multi-layer clouds. However, boundary-layer clouds are very common in the Arctic and, even in the case of multiple-layer clouds, they often contain a liquid-dominated top layer, similar to the two case studies (Mioche et al., 2015). Unfortunately, high cloud layers extending beyond the boundary layer cannot be analyzed with the unpressurized Polar 5 aircraft.

### Changes:

- p2 19: *“Cold air outbreaks occur all year long but they are especially frequent in winter (Kolstad et al., 2009; Fletcher et al., 2016). Warm and moist air masses intruding the Arctic from southern latitudes occur 10 % of the time all year long and are responsible for most of the transport of moisture and heat into the Arctic (Woods et al., 2013; Sedlar and Tjernström, 2017; Pithan et al., 2018)”* was included.

- p7 126: *“Cold air outbreaks and warm air advectons are phenomena often affecting the Arctic regions (Pithan et al., 2018; Sedlar and Tjernström, 2017; Woods et al., 2013; Kolstad et al., 2009; Fletcher et al., 2016). The occurrence of both situations during the ACLOUD campaign make it an ideal testbed to contrast the characteristics of the clouds occurring under each situation.”* was included.

- p22 117 was updated to *“The comparison of both cloud cases highlights the limitations of passive remote sensing alone to identify layered mixed-phase structures if the ice is not sufficiently close to the cloud top. Specially in these cases, the combination of active and passive remote sensing is crucial to fully characterize the horizontal and vertical distribution of ice and liquid particles in mixed-phase clouds.”*

**Were there any Doppler radar data available? Some past studies have shown that the presence of cloud top generating cells frequently occur in the Arctic (as well as in other regions) and could be responsible for some of the horizontal inhomogeneity. If such data are available, perhaps more could be said about the scales of mixing of the phases and their horizontal distributions (and the processes). This would also give more information about the resolution required for analysis.**

Unfortunately, no Doppler radar data are available. In order to detect the low-level Arctic clouds occurring only a few hundred meters above the ground, MiRAC was mounted on Polar 5 with a 25° angle. This increases the vertical resolution and decreases the impact of the ground return, thus reducing the blind zone above the ground (Mech et al., 2019). However, it causes as well a very high horizontal wind component dragging the cloud particles along. This prevents for a reliable estimate of the particle vertical velocity.

**My other concern relates to the use of hexagonal columns to characterize the ice crystals. A lot of previous studies have suggested that the majority of ice crystals in Arctic clouds, including those in mixed-phase conditions, are very irregular and not well characterized by pristine shapes. Can a more realistic assumption about the ice crystal shapes be used? Or, alternatively, there should be more discussion made about the quantitative uncertainties induced by this simplistic assumption.**

It is true that irregular ice crystals are more likely in Arctic mixed-phase clouds. However, from a radiative transfer perspective, we interpret the spectral absorption features of ice crystals. As shown by Ehrlich et al. (2008a,b), the cloud top reflectivity features occurring in the spectral range considered in this study are mainly dominated by the absorption features of the ice, determined in turn by the imaginary part of the refractive index, and the ice crystals effective radius,  $r_{\text{eff}}$ . We tested different non-spherical ice crystal shapes in the radiative transfer simulations presented here and obtained similar results. Accounting for hexagonal columnar ice crystals introduces a negligible bias compared to considering a mixture of ice crystal habits, and does not change the conclusions drawn from the qualitative comparison between measurements and simulations.

Changes:

- p5 118: “*Regarding the phase index, Ehrlich et al. (2008a,b) found that the influence of the ice crystal shape is of minor importance compared to the impact of the particle size. Additional simulations considering different ice crystal habits (not shown here) confirmed this. Hence, the assumption of columns is sufficient to account for the non-sphericity effects of the ice crystals.*” was included.

**Page 4, line 30: It is not true in general that the radar reflectivity for ice is proportional to the sixth power of the ice particle size. For example, Hogan and collaborators have developed much better quantitative models for converting ice crystal particle size distributions to radar reflectivity.**

We are sorry for this unprecise phrasing. We meant that the radar reflectivity is proportional to the sixth moment of the particle size distribution (Hogan and O’Conner, 2004) and thus, it is more sensitive to large particles, which are likely to be ice crystals. Since lidar signals are more sensitive to smaller and populous particles like liquid water droplets, Shupe (2007) and Kalesse et al. (2016) point towards a synergetic use of lidar and radar measurements to identify different in-cloud phase regimes similar to what presented here.

Changes:

- p5 13 was updated to “*The radar reflectivity is proportional to the sixth power of the particle size distribution, and thus, is most sensitive to large particles, such as ice crystals (Hogan and O’Conner, 2004; Shupe, 2007; Kalesse et al., 2016). Therefore, it is used as an indicator of the vertical location of large ice crystals in mixed-phase clouds.*”

**Page 5, line 8: How can the standard profile be used in combination with the dropsonde data? Wouldn't one or the other have to be used to give the vertical profile?**

The dropsonde data does not provide all the parameters required for the radiative transfer simulations. By combining the dropsonde data with the standard atmospheric profiles, libRadtran makes use of the measured pressure, temperature, and humidity profiles and scales the gas species concentrations ( $O_3$ ,  $NO_2$ ,  $BrO$ ,  $ClO_2$ ,  $CH_2O$ ,  $SO_2$ , and  $O_4$ ) of the standard atmospheric profile to the measured pressure.

**Page 6, line 3: What are unrealistic values of LWP? This should be more quantitative.**

Shupe et al. (2006), Mioche et al. (2017), Nomokonova et al. (2019) and Gierens et al. (2019) report values of the *LWP* rarely exceeding  $100 \text{ g m}^{-2}$ , with mean values between 30 and  $50 \text{ g m}^{-2}$ . Therefore, we conclude that the retrieved values based on the measurements of AISA Hawk (in average  $270 \text{ g m}^{-2}$ ) are caused by a retrieval bias due to the existence of ice in the considered clouds.

Changes:

- p6 l10: “*Past observations show that the LWP of typical Arctic boundary-layer clouds is on average 30 -  $50 \text{ g m}^{-2}$  and rarely exceeds  $100 \text{ g m}^{-2}$  (Shupe et al., 2006; Mioche et al., 2017; Nomokonova et al., 2019; Gierens et al., 2019)*” was included.

**Page 6, line 6: What quantitative criteria were used to identify the presence of cold air outbreaks?**

The synoptic conditions during ACLOUD were analyzed by Knudsen et al. (2018). Within their study, the Marine Cold Air Outbreak (MCAO) index is analyzed. Similar to Kolstad (2017) and Papritz et al. (2015), the MCAO index is based on the difference between the surface and the 850 hPa potential temperature, which was calculated every 6 hours during the ACLOUD period. Whereas positive values of the MCAO index were used to identify cold air outbreak events, strong negative values of the MCAO index with respect to the climatology identified warm air advection events. Based on this analysis, Knudsen et al. (2018) divided the ACLOUD period into a cold period (between 23 and 29 May 2017, characterized by positive values of the MCAO index), a warm period (between 30 May and 12 June 2017, with values of the MCAO index well below the climatology) and a normal period (between 13 and 26 June 2017, where the MCAO index acquired similar values to the climatology).

**Page 7, line 6: Why couldn't it also be attributed to a reduced concentration of particles rather than just small particles?**

This is correct, a reduced concentration of particles would lead to a similar effect. Thanks for pointing on this insufficient explanation.

Changes:

- p8 l18 was updated to “*either to smaller ice crystals or to a reduced particle concentration*”.

**Additional changes:**

- p4 17 now includes “Among the in-situ probes installed on Polar 6, the Small Ice Detector (SID-3, Vochezer et al., 2016) provides the particle size distribution of hydrometeors with sizes between  $5\mu\text{m}$  and  $45\mu\text{m}$ ”.
- The beginning of Section 3.2.2 was updated to “Mixed-phase clouds in the Arctic commonly consist of a single layer of supercooled liquid water droplets at cloud top, from which ice crystals precipitate (Mioche et al., 2015), which is in line with the radar/lidar observations presented in Fig. 3. Additionally, Ehrlich et al. (2009) found evidence of ice crystals near the cloud top. Horizontal inhomogeneities in the vertical distribution of the liquid water and ice occur in horizontal scales of 10 m (Korolev and Isaac, 2006; Lawson et al., 2010) and are expected to relate to the small-scale structures (i.e., holes and domes) on the cloud top. Therefore, reproducing the observed trends of  $R_{1240}$  and  $\mathcal{I}_s$  with simulated mixed-phase clouds can provide information about the horizontal distribution of the cloud thermodynamic phase vertical structure.”
- Style edition and typographic error correction were applied to the whole manuscript.

## References

- Dipankar, A., Stevens, B., Heinze, R., Moseley, C., Zängl, G., Giorgetta, M., and Brdar, S.: Large eddy simulation using the general circulation model ICON, *J. Adv. Model. Earth Sy.*, 7, 963–986, <https://doi.org/10.1002/2015MS000431>, 2015.
- Ehrlich, A., Bierwirth, E., Wendisch, M., Gayet, J.-F., Mioche, G., Lampert, A., and Heintzenberg, J.: Cloud phase Identification of Arctic boundary-layer clouds from airborne spectral reflection measurements: test of three approaches, *Atmos. Chem. Phys.*, <https://doi.org/10.5194/acp-8-7493-2008>, 2008a.
- Ehrlich, A., Wendisch, M., Bierwirth, E., Herber, A., and Schwarzenböck, A.: Ice crystal shape effects on solar radiative properties of Arctic mixed-phase clouds - Dependence on microphysical properties, *Atmos. Res.*, 88, 266–276, 2008b.
- Ehrlich, A., Wendisch, M., Bierwirth, E., Gayet, J.-F., Mioche, G., Lampert, A., and Mayer, B.: Evidence of ice crystals at cloud top of Arctic boundary-layer mixed-phase clouds derived from airborne remote sensing, *Atmos. Chem. Phys.*, 9, 9401–9416, <https://doi.org/10.5194/acp-9-9401-2009>, 2009.
- Emde, C., Buras-Schnell, R., Kylling, A., Mayer, B. and Gasteiger, J., Hamann, U., Kylling, J., Richter, B., Pause, C., Dowling, T., and Bugliaro, L.: The libRadtran software package for radiative transfer calculations (version 2.0.1), *Geosci. Model Dev.*, <https://doi.org/10.5194/gmd-9-1647-2016>, 2016.
- Fletcher, J., Mason, S., and Jakob, C.: The Climatology, Meteorology, and Boundary Layer Structure of Marine Cold Air Outbreaks in Both Hemispheres, *J. Climate*, 29, 1999–2014, <https://doi.org/10.1175/JCLI-D-15-0268.1>, 2016.
- Gierens, R., Kneifel, S., Shupe, M. D., Ebell, K., Maturilli, M., and Löhnert, U.: Low-level mixed-phase clouds in a complex Arctic environment, *Atmos. Chem. Phys. Discuss.*, 2019, 1–37, <https://doi.org/10.5194/acp-2019-610>, 2019.
- Gutleben, M., Groß, S., and Wirth, M.: Cloud macro-physical properties in Saharan-dust-laden and dust-free North Atlantic trade wind regimes: a lidar case study, *Atmos. Chem. And Phys.*, 19, 10659–10673, <https://doi.org/10.5194/acp-19-10659-2019>, 2019.
- Heinze, R., Dipankar, A., Henken, C. C., Moseley, C., Sourdeval, O., Trömel, S., Xie, X., Adamidis, P., Ament, F., Baars, H., Barthlott, C., Behrendt, A., Blahak, U., Bley, S., Brdar, S., Brueck, M., Crewell, S., Deneke, H., Girolamo, P. D., Evaristo, R., Fischer, J., Frank, C., Friederichs, P., Göcke, T., Gorges, K., Hande, L., Hanke, M., Hansen, A., Hege, H., Hoose, C., Jahns, T., Kalthoff, N., Klocke, D., Kneifel, S., Knippertz, P., Kuhn, A., Laar, T. v., Macke, A., Maurer, V., Mayer, B., Meyer, C. I., Muppa, S. K., Neggens, R. A. J., Orlandi, E., Pantillon, F., Pospichal, B., Röber, N., Scheck, L., Seifert, A., Seifert, P., Senf, F., Siligam, P., Simmer, C., Steinke, S., Stevens, B., Wapler, K., Weniger, M., Wulfmeyer, V., Zängl, G., Zhang, D., and Quaas, J.: Large-eddy simulations over Germany using ICON: a comprehensive evaluation, *Q. J. Royal Met. Soc.*, 143, 69–100, <https://doi.org/10.1002/qj.2947>, 2017.
- Hogan, R. J. and O’Conner, E.: Facilitating cloud radar and lidar algorithms: the Cloudnet Instrument Synergy/Target Categorization Product, Dept. of Meteorol. Univ of Reading, UK, URL <http://www.met.reading.ac.uk/~swrhgnrj/publications/categorization.pdf>, 2004.
- Kalesse, H., de Boer, G., Solomon, A., Oue, M., Ahlgrimm, M., Zhang, D., Shupe, M. D., Luke, E., and Protat, A.: Understanding Rapid Changes in Phase Partitioning between Cloud Liquid and Ice in Stratiform Mixed-Phase Clouds: An Arctic Case Study, *Mon. Wea. Rev.*, 144, 4805–4826, <https://doi.org/10.1175/MWR-D-16-0155.1>, 2016.

- Knudsen, E. M., Heinold, B., Dahlke, S., Bozem, H., Crewell, S., Gorodetskaya, I. V., Heygster, G., Kunkel, D., Maturilli, M., Mech, M., Viceto, C., Rinke, A., Schmithüsen, H., Ehrlich, A., Macke, A., Lüpkes, C., and Wendisch, M.: Meteorological conditions during the ACLOUD/PASCAL field campaign near Svalbard in early summer 2017, *Atmos. Chem. Phys.*, 18, 17 995–18 022, <https://doi.org/10.5194/acp-18-17995-2018>, 2018.
- Kolstad, E. W.: Higher ocean wind speeds during marine cold air outbreaks, *Q.J.R. Meteorol. Soc.*, 143, 2084–2092, <https://doi.org/10.1002/qj.3068>, 2017.
- Kolstad, E. W., Bracegirdle, T. J., and Seierstad, I. A.: Marine cold-air outbreaks in the North Atlantic: temporal distribution and associations with large-scale atmospheric circulation, *Climate Dyn.*, 33, 187–197, 2009.
- Korolev, A. and Isaac, G. A.: Relative humidity in liquid, mixed-phase, and ice clouds, *J. Atmos. Sci.*, 63, 2865–2880, <https://doi.org/10.1175/JAS3784.1>, 2006.
- Langenbach, A., Baumgarten, G., Fiedler, J., Lübken, F.-J., von Savigny, C., and Zalach, J.: Year-round stratospheric aerosol backscatter ratios calculated from lidar measurements above northern Norway, *Atmos. Meas. Tech.*, 12, 4065–4076, <https://doi.org/10.5194/amt-12-4065-2019>, 2019.
- Lawson, R. P., Jensen, E., Mitchell, D. L., Baker, B., Mo, Q. X., and Pilson, B.: Microphysical and radiative properties of tropical clouds investigated in TC4 and NAMMA, *J. Geophys. Res.*, 115, D00J08, <https://doi.org/10.1029/2009JD013017>, 2010.
- Lucy, L. B.: An iterative technique for the rectification of observed distributions, *Astron. J.*, 79, 745, <https://doi.org/10.1086/111605>, 1974.
- Mayer, B. and Kylling, A.: Technical note: The *libRadtran* software package for radiative transfer calculations - description and examples of use, *Atmos. Chem. Phys.*, 5, 1855–1877, <https://doi.org/10.5194/acp-5-1855-2005>, 2005.
- Mech, M., Kliesch, L.-L., Anhäuser, A., Rose, T., Kollias, P., and Crewell, S.: Microwave Radar/radiometer for Arctic Clouds MiRAC: First insights from the ACLOUD campaign, *Atmos. Meas. Tech.*, 2019, 1–32, <https://doi.org/10.5194/amt-12-5019-2019>, 2019.
- Mioche, G., Jourdan, O., Ceccaldi, M., and Delanoë, J.: Variability of mixed-phase clouds in the Arctic with a focus on the Svalbard region: a study based on spaceborne active remote sensing, *Atmos. Chem. Phys.*, 15, 2445–2461, <https://doi.org/10.5194/acp-15-2445-2015>, 2015.
- Mioche, G., Jourdan, O., Delanoë, J., Gourbeyre, C., Febvre, G., Dupuy, R., Monier, M., Szczap, F., Schwarzenboeck, A., and Gayet, J.-F.: Vertical distribution of microphysical properties of Arctic springtime low-level mixed-phase clouds over the Greenland and Norwegian seas, *Atmos. Chem. Phys.*, 17, 12 845–12 869, <https://doi.org/10.5194/acp-17-12845-2017>, 2017.
- Nomokonova, T., Ebell, K., Löhnert, U., Maturilli, M., Ritter, C., and O’Connor, E.: Statistics on clouds and their relation to thermodynamic conditions at Ny-Ålesund using ground-based sensor synergy, *Atmos. Chem. Phys.*, 19, 4105–4126, <https://doi.org/10.5194/acp-19-4105-2019>, 2019.
- Papritz, L., Pfahl, S., Sodemann, H., and Wernli, H.: A Climatology of Cold Air Outbreaks and Their Impact on Air–Sea Heat Fluxes in the High-Latitude South Pacific, *J. Climate*, 28, 342–364, <https://doi.org/10.1175/JCLI-D-14-00482.1>, 2015.
- Pithan, F., Svensson, G., Caballero, R., Chechin, D., Cronin, T. W., Ekman, A. M. L., Neggers, R., Shupe, M. D., Solomon, A., Tjernström, M., and Wendisch, M.: Role of air-mass transformations in exchange between the Arctic and mid-latitudes, *Nat. Geosci.*, 11, 805–812, <https://doi.org/10.1038/s41561-018-0234-1>, 2018.

- Richardson, W. H.: Bayesian-Based Iterative Method of Image Restoration, *J. Opt. Soc. Am.*, 62, 55–59, <https://doi.org/10.1364/JOSA.62.000055>, 1972.
- Schäfer, M., Bierwirth, E., Ehrlich, A., Heyner, F., and Wendisch, M.: Retrieval of cirrus optical thickness and assessment of ice crystal shape from ground-based imaging spectrometry, *Atmos. Meas. Tech.*, 6, 1855–1868, <https://doi.org/10.5194/amt-6-1855-2013>, 2013.
- Schemann, V. and Ebell, K.: Simulation of mixed-phase clouds with the ICON large-eddy model in the complex Arctic environment around Ny-Ålesund, *Atmos. Chem. Phys.*, 20, 475–485, <https://doi.org/10.5194/acp-20-475-2020>, 2020.
- Sedlar, J. and Tjernström, M.: Clouds, warm air, and a climate cooling signal over the summer Arctic, *Geophys. Res. Lett.*, 44, 1095–1103, <https://doi.org/10.1002/2016GL071959>, 2017.
- Shupe, M. D.: A ground-based multisensor cloud phase classifier, *Geophys. Res. Lett.*, 34, L22 809, 2007.
- Shupe, M. D., Matrosov, S. Y., and Uttal, T.: Arctic mixed-phase cloud properties derived from surface-based sensors at SHEBA, *J. Atmos. Sci.*, 63, 697–711, <https://doi.org/10.1175/JAS3659.1>, 2006.
- Vochezer, P., Järvinen, E., Wagner, R., Kupiszewski, P., Leisner, T., and Schnaiter, M.: In situ characterization of mixed phase clouds using the Small Ice Detector and the Particle Phase Discriminator, *Atmos. Meas. Tech.*, 9, 159–177, <https://doi.org/10.5194/amt-9-159-2016>, 2016.
- Wang, S., Zheng, X., and Jiang, Q.: Strong sheared stratocumulus convection: An observationally based large-eddy simulation study, *Atmos. Chem. Phys.*, 12, 5223–5235, 2012.
- Woods, C., Caballero, R., and Svensson, G.: Large-scale circulation associated with moisture intrusions into the Arctic during winter, *Geophys. Res. Lett.*, 40, 4717–4721, <https://doi.org/10.1002/grl.50912>, 2013.
- Zinner, T., Mayer, B., and Schröder, M.: Determination of 3D cloud structures from high resolution radiance data, *J. Geophys. Res.*, 111, doi:10.1029/2005JD006 062, 2006.

# Small-scale structure of thermodynamic phase in Arctic mixed-phase clouds observed by airborne remote sensing during a cold air outbreak and a warm air advection event

Elena Ruiz-Donoso<sup>1</sup>, André Ehrlich<sup>1</sup>, Michael Schäfer<sup>1</sup>, Evelyn Jäkel<sup>1</sup>, Vera Schemann<sup>2</sup>, Susanne Crewell<sup>2</sup>, Mario Mech<sup>2</sup>, Birte Solveig Kulla<sup>2</sup>, Leif-Leonard Kliesch<sup>2</sup>, Roland Neuber<sup>3</sup>, and Manfred Wendisch<sup>1</sup>

<sup>1</sup>Leipzig Institute for Meteorology (LIM), University of Leipzig, Germany

<sup>2</sup>Institute for Geophysics and Meteorology, University of Cologne, Germany

<sup>3</sup>Alfred-Wegener-Institut Helmholtz Center for Polar and Marine Research (AWI), Germany

**Correspondence:** Elena Ruiz-Donoso (elena.ruiz\_donoso@uni-leipzig.de)

**Abstract.** The ~~synergy-between-combination of downward-looking~~ airborne lidar, radar, ~~passive~~ microwave, and ~~passive~~ imaging spectrometer measurements was ~~used-exploited~~ to characterize the vertical and small-scale (down to 10 m) horizontal distribution of the ~~cloud-thermodynamic-phase~~. ~~Two case studies-thermodynamic phase~~ of low-level Arctic ~~clouds-mixed-layer clouds~~. ~~Two cloud cases observed~~ in a cold air outbreak and a warm air advection ~~event~~ observed during the Arctic CLOUD Observations Using Airborne Measurements during Polar Day (ACLOUD) ~~campaign~~ were investigated. Both ~~clouds-cloud cases~~ exhibited the typical vertical mixed-phase structure with mostly liquid water droplets at cloud top and ice crystals in lower layers. The ~~cloud-top-horizontal~~horizontal, small-scale ~~variability-distribution of the thermodynamic phase as~~ observed during the cold air outbreak is dominated by the liquid water close to the cloud top and shows no indication of ice in lower cloud layers. Contrastingly, the cloud top variability of the case observed during a warm air advection showed some ice in areas of low reflectivity or cloud holes. Radiative transfer simulations considering homogeneous mixtures of liquid water droplets and ice crystals were able to reproduce the horizontal variability of this warm air advection. ~~To account for more realistic vertical distributions of the thermodynamic phase, large~~ Large eddy simulations (LES) were performed to reconstruct the observed cloud properties ~~and were used~~, ~~which were used subsequently~~ as input for radiative transfer simulations. The ~~LES~~ simulations of the cloud ~~case~~ observed during the cold air outbreak, with mostly liquid water at cloud top, realistically reproduced the observations. For the warm air advection case, the simulated ~~cloud-field-underestimated the~~ ice water content (~~AWC-IWC~~) ~~was systematically lower than the measured IWC~~. Nevertheless, ~~it the~~ LES simulations revealed the presence of ice particles close to the cloud top and confirmed the observed horizontal variability of the cloud field. It is concluded that the cloud top small-scale horizontal variability ~~reacts-is directly linked~~ to changes in the vertical distribution of the cloud thermodynamic phase. Passive satellite-borne imaging spectrometer observations with pixel sizes larger than 100 m miss the small-scale cloud top structures, ~~which limits their capabilities to provide indications about the cloud-vertical structure~~.

## 1 Introduction

In the Arctic, low-level stratus and stratocumulus clouds are present around 40 % of the time on annual average (Shupe et al., 2006; Shupe, 2011) and they may persist up to several weeks (Shupe, 2011; Morrison et al., 2012). At least 30 % of these clouds are of mixed-phase type (Mioche et al., 2015). Their radiative properties and life ~~eye~~cycles are determined by the partitioning and ~~stratification~~the spatial (vertical/horizontal) distribution of liquid water droplets and ice crystals. Therefore, mixed-phase cloud properties ~~contribute to are important for~~ the characteristics of the Arctic climate system ~~, and make it particularly sensitive to climate change (Tan and Storelvmo, 2019). In that way, mixed-phase clouds (Tan and Storelvmo, 2019). They~~ are suspected to play ~~a~~an important role in the accelerated warming relative to lower latitudes observed in the last decades, a phenomenon known as Arctic amplification (Serreze and Barry, 2011; Wendisch et al., 2017). The microphysical and optical properties of Arctic mixed-phase clouds are determined by a complex network of feedback mechanisms between local and large-scale dynamical and microphysical processes (e.g., Morrison et al., 2012; Mioche et al., 2017). Large-scale advection of air masses across the Arctic predefine their general nature (Pithan et al., 2018). In case of cold air masses advected from the central Arctic region towards lower latitudes, the cold air transported over the warm ocean surface produces intense shallow convection and characteristic cloud street structures, which may extend over several hundred kilometers. Cold air outbreaks occur all year long, but they are especially frequent in winter (Kolstad et al., 2009; Fletcher et al., 2016). Warm and moist air masses intruding into the Arctic from southern latitudes ~~rapidly cool~~occur 10 % of the time all year long and are responsible for most of the transport of moisture and heat into the Arctic (Woods et al., 2013; Sedlar and Tjernström, 2017; Pithan et al., 2018). During the northward transport, important air mass transformations take place. The air rapidly cools close to the surface, leading to shallow but strong temperature inversions ~~and~~ promoting low-level, persistent clouds (Sedlar and Tjernström, 2017; Tjernström et al., 2015). In these clouds, the vertical motion is driven mainly by radiative cooling at cloud top. ~~The cores of the convective cells arising in Arctic clouds~~ As a consequence, convective cells appear in intervals of several kilometers (Shupe et al., 2008; Roesler et al., 2017). On smaller scales of a few hundred meters, the vertical motion is additionally ~~determined~~driven by evaporative cooling, associated with entrainment of moist air supplied from upper layers (Mellado, 2017). This entrainment process ensures the formation of liquid water droplets and balances the loss of cloud water by precipitating ice crystals (Korolev, 2007; Shupe et al., 2008; Morrison et al., 2012). Observations by Schäfer et al. (2017, 2018) show that the small-scale horizontal inhomogeneities of updrafts and downdrafts have typical length scales down to 60 m. In downdraft regions, the Wegener-Bergeron-Findeisen process may dominate over the nucleation of liquid water droplets ~~(Korolev and Field, 2008)~~(Korolev and Field, 2008; Korolev et al., 2017), causing the ice crystals to grow at the expense of the liquid water droplets.

Interactions between these processes determine the structure of the cloud, both vertically and horizontally. The cloud thermodynamic phase ~~organizes~~develops vertically in specific patterns. Most frequently, a liquid-water-dominated layer is observed from which ice crystals precipitate ~~is observed~~ (Shupe et al., 2006; McFarquhar et al., 2007; Ehrlich et al., 2009; Mioche et al., 2015). Spatial differences of the cloud phase vertical distribution can, in turn, occur ~~in~~on horizontal scales down to tens of meters (Korolev and Isaac, 2006; Lawson et al., 2010). Therefore, understanding the radiative properties and temporal evolu-

tion of Arctic mixed-phase clouds requires a three-dimensional (3D) characterization of the thermodynamic phase partitioning, which relates the vertical distribution of liquid droplets and ice crystals to the small scale structures observed ~~on-close to~~ the cloud top.

The analysis of small-scale microphysical inhomogeneities of Arctic stratus is challenging. Global climate models (GCMs) typically have horizontal and vertical grid sizes of 100 km and 1 km, respectively (Tan and Storelvmo, 2016). Global reanalysis products are provided with a horizontal grid that is typically larger than 40 km (Lindsay et al., 2014). This coarse resolution cannot resolve in-cloud microphysical and dynamical processes, such as the updraft and downdraft motions. Therefore, these processes need to be parameterized (Field et al., 2004; Klein et al., 2009). Cloud resolving models (1 km horizontal and 30 m vertical resolution; Luo et al., 2008), and large eddy simulations (LES, below 100 m horizontal and 15 m vertical resolution; Loewe et al., 2017) resolve small-scale cloud processes and are used to improve the GCMs subgrid mixed-phase cloud parameterization. In order to evaluate the performance of these high resolution simulations, ~~high-resolution-adequately resolved~~ observations are needed (Werner et al., 2014; Roesler et al., 2017; Schäfer et al., 2018; Egerer et al., 2019; Neggers et al., 2019; Schemann and Ebell, 2020).

In the past, the observation of the thermodynamic phase transitions associated with small-scale cloud structures down to scales of 10 m was challenging due to limitations of the measurement methods. Passive and active satellite-borne remote sensing techniques have typical resolutions coarser than 250 m (Stephens et al., 2002). Ground-based active cloud remote sensing methods (lidar and radar), with vertical resolution of about 50 m and averaging intervals of 10 s (Kollias et al., 2007; Maahn et al., 2015), ~~mostly~~ point only in zenith direction and ~~miss horizontal two-dimensional information on~~ ~~thus may miss horizontal~~ inhomogeneities (Marchand et al., 2007). Similarly, airborne in situ measurements of cloud microphysical properties require averaging periods of at least 1 s, integrating over scales of 50 m at a typical flight speed of 50 m s<sup>-1</sup> (Mioche et al., 2017), and therefore, potentially mix individual pockets of ice crystals and liquid water droplets. Airborne active radar and lidar measurements also average over along-track distances of about 50 m (1 s at 50 m s<sup>-1</sup> flight speed; Stachlewska et al., 2010; Mech et al., 2019). Airborne imaging remote sensing techniques have the potential to map the cloud top geometry : ~~Reflected-solar in high spatial resolution. Solar~~ radiation measurements by spectral imagers provide ~~an-enhanced-data with~~ ~~an~~ spatial resolution of down to a few meters. Based on this measurement approach, Schäfer et al. (2013) and Bierwirth et al. (2013) retrieved two-dimensional (2D) fields of cloud optical thickness resolving changes in spatial scales smaller than 50 m, which are associated with the evaporation of cloud particles in downdraft regions. For selected cases, Thompson et al. (2016) illustrated the potential of spectral imagers to retrieve 2D fields of cloud thermodynamic phase. The identification of mixed-phase cloud regions, however, was based on the assumption of homogeneously mixed clouds and did not consider the vertical distributions of the ice ~~and liquid particles~~ ~~crystals and liquid water droplets~~. Due to the passive nature of the imaging spectrometers, the measurements integrate over the entire cloud column, ~~but-although they~~ are dominated by the cloud properties close to the cloud top (Platnick, 2000). They commonly cannot resolve the clouds vertically. Therefore, to avoid ~~misclassifications~~ ~~misclassifications~~, the information about the cloud vertical structure provided by active remote sensing is needed to interpret passive remote sensing measurements of reflected solar radiation.

This study ~~makes use of~~ exploits combined passive spectral imaging techniques and active remote sensing measurements (radar and lidar) to characterize the cloud phase partitioning in the 3D cloud structure. The active remote sensing instruments provide the general vertical stratification of ice particles and liquid water droplets, which is needed to interpret the 2D maps of cloud phase observed by the spectral imager. Two mixed-phase cloud cases ~~observed~~ detected during the Artic CLOUD Observations Using airborne measurements during polar Day (ACLOUD) campaign are chosen to demonstrate this instrument synergy (Wendisch et al., 2019). Section 2 introduces the instrumentation ~~and~~, the retrieval approach to derive 2D maps of cloud phase, and the LES simulations. The two case studies are presented in ~~Seet.~~ Section 3, including a discussion of the impact of the cloud vertical structure on the cloud phase retrieval. The observation are compared to LES simulations in ~~Seet.~~ Section 4. The information loss due to the smoothing of the fine-scale cloud structures to the typical geometry obtained by satellite-borne remote sensing is quantified in ~~Seet.~~ Section 5.

## 2 Methods

### 2.1 Observations

The ACLOUD campaign was performed to improve the understanding of the role of Arctic low and mid-level clouds in Arctic amplification; it took place in the vicinity of the Svalbard archipelago in May and June 2017 (Wendisch et al., 2019; Ehrlich et al., 2019). During ACLOUD, active and passive remote sensing instruments and in-situ probes were operated on the research ~~aircrafts~~ aircraft Polar 5 and Polar 6 of the Alfred Wegener Institute Helmholtz-Center for Polar and Marine Research (AWI; Wesche et al., 2016). Among the in-situ probes installed on Polar 6, the Small Ice Detector (SID-3, Vochezer et al., 2016) provides the particle size distribution of hydrometeors with sizes between 5  $\mu\text{m}$  and 45  $\mu\text{m}$ . The passive remote sensing equipment installed on Polar 5 included, among others, the AISA Hawk spectral imager (Pu, 2017). The downward-viewing ~~pushboom~~ pushboom sensor of AISA Hawk is aligned across-track to ~~generate~~ measure 2D fields of upward radiance ( $I_{\lambda}^{\uparrow}$ ) reflected by the cloud and surface. Considering uncertainties due to the calibration and noise in the measured signal, the uncertainty in the measured radiance is estimated to be in the range of 6% (Schäfer et al., 2013). With 384 across-track pixels, a 36° field of view (FOV) and a typical vertical distance between aircraft and cloud top of 1 km, AISA Hawk samples with a spatial resolution of roughly 2 m. At this resolution, horizontal photon transport needs to be taken into account. The AISA Hawk measurements have been corrected from this effect using the deconvolution algorithm introduced in App. A. Each pixel contains spectral ~~information~~ measurements between 930 nm and 2550 nm wavelength ~~distributed~~ in 288 channels with an average spectral resolution (full width at half maximum, FWHM) of about 10 nm. More details on the calibration of AISA Hawk and the data processing are presented by Ehrlich et al. (2019). Two-dimensional fields of spectral cloud top reflectivity ( $R_{\lambda}$ ) are obtained by combining reflected radiance fields, detected by AISA Hawk, with simultaneous measurements of the downward spectral irradiance ( $F_{\lambda}^{\downarrow}$ ) obtained by the Spectral Modular Airborne Radiation measurement system (SMART; Wendisch et al., 2001; Ehrlich et al., 2019):

$$R_{\lambda} = \pi \cdot \frac{I_{\lambda}^{\uparrow}}{F_{\lambda}^{\downarrow}}. \quad (1)$$

The cloud top reflectivity  $R_\lambda$  in the spectral region-range between  $\lambda_a = 1550$  nm and  $\lambda_b = 1700$  nm, characterized by the different absorption features of liquid water and ice, is used to discriminate the cloud thermodynamic phase (Pilewski and Twomey, 1987; Chylek and Borel, 2004; Jäkel et al., 2013; Thompson et al., 2016). The spectral differences in the cloud top reflectivity of pure liquid and pure ice clouds are illustrated in Fig. 1. To identify the cloud phase, Ehrlich et al. (2008a) defined the slope phase index ( $\mathcal{I}_s$ ), which quantifies the spectral slope of the cloud top reflectivity in this spectral region and is sensitive to the amount of ice crystals and liquid water droplets close to cloud top:

$$\mathcal{I}_s = 100 \cdot \frac{(\lambda_b - \lambda_a)}{R_{1640}} \left( \frac{dR_\lambda}{d\lambda} \right) \frac{(\lambda_b - \lambda_a)}{R_{1640}} \left( \frac{dR_\lambda}{d\lambda} \right)_{[\lambda_a, \lambda_b]}. \quad (2)$$

A threshold value for the slope phase index of 20 discriminates between pure liquid water ( $\mathcal{I}_s < 20$ ) and pure ice or mixed-phase ( $\mathcal{I}_s > 20$ ) close to cloud top (Ehrlich et al., 2009). By applying Eq. (2) to the AISA Hawk measurements, fields of  $\mathcal{I}_s$  are obtained, which spatially generated, which resolve the horizontal distribution of the thermodynamic phase of the cloud uppermost 200 m layer, typically corresponding to an in-cloud optical depth of about 5 (Platnick, 2000; Ehrlich, 2009; Miller et al., 2014).

The vertical distribution of the cloud thermodynamic phase is retrieved from measurements by the Microwave Radar/radiometer for Arctic Clouds (MiRAC; Mech et al., 2019) and the Airborne Mobile Aerosol Lidar (AMALi; Stachlewska et al., 2010) deployed in parallel with the AISA Hawk sensor on board of Polar 5. The radar reflectivity is proportional to the sixth power of the particle size distribution, and thus, is most sensitive to large particles, such as ice crystals (Hogan and O’Conner, 2004; Shupe, 2004). Therefore, it is used to identify as an indicator of the vertical location of large ice crystals in mixed-phase clouds. Contrastingly In contrast, the AMALi backscatter signal is strongly attenuated by high concentrations of small particles and, thus, identifies the location of small supercooled liquid water droplets close to the cloud top in mixed-phase clouds.

## 2.2 Radiative transfer modelling

Radiative transfer simulations are employed to interpret-interpret the horizontal structure of the cloud-slope phase index, and to retrieve 2D fields of cloud optical thickness ( $\tau$ ) and effective radius ( $r_{\text{eff}}$ ). They were performed with the Library for Radiative transfer (libRadtran) code (Mayer and Kylling, 2005; Emde et al., 2016). The simulations applied the radiative transfer solver FDISORT2 (Discrete Ordinate Radiative Transfer) introduced by Stamnes et al. (2000). The standard subarctic summer-atmospheric sub-Arctic summer atmospheric profile provided by libRadtran was employed, together with temperature and water vapor profiles measured by dropsondes released during the respective flights close to the measurement sites. A maritime aerosol type and the surface albedo of open ocean were selected (Shettle, 1990). The solar zenith angle (SZA) was adjusted to the location and time of each specific measurement. The simulations of liquid water clouds assumed the validity of Mie theory, whereas those including ice clouds assumed columnar ice crystals and applied the “Hey” parameterization, based on Yang et al. (2000) to convert microphysical into optical properties. Regarding the phase index, Ehrlich et al. (2008a, b) found that the influence of the ice crystal shape is of minor importance compared to the impact of the particle size, which was confirmed by additional simulations considering different ice crystal habits (not shown here). Hence, the assumption of columns is sufficient to account for the non-sphericity effects of the ice crystals.

In a first step, extending the work of Bierwirth et al. (2013) and Schäfer et al. (2013) to the near infrared spectral ~~region, the~~ range, the spectral cloud top reflectivity fields measured by AISA Hawk ~~are-were~~ used to retrieve fields of optical thickness and effective radius. For this purpose, the reflectivity  $R_{1240}$  at a ~~scattering~~-wavelength of 1240 nm (scattering dominated), sensitive to the cloud optical thickness, is combined with  $R_{1625}$  at ~~an-absorbing-a~~ wavelength of 1625 nm, where absorption of solar  
 5 radiation dominates and influenced mainly by the particle size (Nakajima and King, 1990). The ~~position of these wavelenghts~~ location of these wavelenghts in the cloud top reflectivity spectrum is shown in Fig. 1. To reduce the retrieval uncertainties, the radiance ratio approach by Werner et al. (2013) was applied. Look-up tables considering the ~~sun-sensor-sensor~~ viewing geometry of every pixel of AISA Hawk are simulated for various combinations of cloud optical thickness and effective radius. For the simulations, pure liquid water clouds are assumed. ~~In the presence~~ Therefore, in the case of mixed-phase clouds, ~~this~~  
 10 ~~might bias the retrieved~~ the retrieved values of optical thickness and effective radius might be biased. However, since Arctic low-level mixed-phase clouds are typically topped by a liquid-water layer (Shupe et al., 2006; McFarquhar et al., 2007), the associated uncertainties are expected to be lower than the variability within the cloud field.

The retrieved optical thickness and effective radius, assuming a plane-parallel 1D radiative transfer model, are affected by 3D radiative effects (Zinner and Mayer, 2006; Marshak et al., 2006). While the 3D nature of the cloud structures will cause  
 15 an overestimation of the optical thickness in the ~~bright-brightly~~ illuminated areas, the effective radius is overestimated in the shadowed regions. Horváth et al. (2014) showed that, due to their opposite sign, the 3D bias of retrieved optical thickness and effective radius partially cancel when calculating the liquid water path *LWP*. Therefore, the retrieved fields of  $\tau$  and  $r_{\text{eff}}$  are converted into fields of *LWP* using the relation by Kokhanovsky (2004):

$$LWP = \frac{2}{3} \cdot \rho \cdot \tau \cdot r_{\text{eff}}. \quad (3)$$

20 As it was the case for the retrieved  $\tau$  and  $r_{\text{eff}}$ , this conversion assumes liquid water clouds with a homogeneously mixed ~~vertical~~ vertically constant profile. Considering a homogeneous vertical profile may result in inaccuracies even for pure liquid water clouds (Zhou et al., 2016). Mixed-phase clouds, in addition, violate the pure-phase assumption. The presence of ice crystals introduces ~~an-a significant~~ error in the calculated ~~LWP~~ LWP, which reaches values well above the typical values observed in Arctic pure liquid water clouds. Past observations show that the LWP of typical Arctic boundary-layer clouds is in the range of  
 25 30 - 50 g m<sup>-2</sup> and rarely exceeds 100 g m<sup>-2</sup>, (Shupe et al., 2006; Mioche et al., 2017; Nomokonova et al., 2019; Gierens et al., 2019). Appendix A analyzes the different impact of shades and inhomogeneous thermodynamic phase distributions in the retrieved LWP. In this paper, unrealistically high retrieved *LWP* values are used to identify mixed-phase clouds.

### 2.3 Large Eddy Simulations (LES)

Simulations using the ICOSahedral Non-hydrostatic atmosphere model (ICON), operated in its Large Eddy Model (LEM)  
 30 configuration (Heinze et al., 2017; Dipankar et al., 2015), provide a quantitative view into the cloud vertical structure. The simulated cloud vertical profiles were used as input for radiative transfer simulations to analyze the impact of different vertical distributions of the cloud thermodynamic phase on the cloud top horizontal variability.

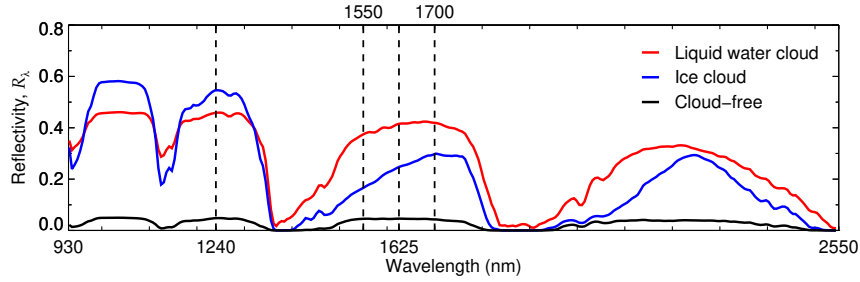


**Figure 1.** Reflectivity spectra of a pure liquid water cloud and a pure ice cloud of optical thickness 12 compared with a clear sky spectrum in the wavelength range measured by AISA Hawk. The vertical dashed lines indicate the wavelengths needed to calculate the slope phase index (1550 - 1700 nm), and to retrieve the cloud optical thickness (1240 nm) and effective radius (1625 nm)

ICON-LEM simulations were forced by initial and lateral boundary conditions from the European Centre for Medium-Range Weather Forecasts (ECMWF) Integrated Forecast System (IFS; Gregory et al., 2010). The simulations were performed in a one-way nested setup with a 600 m spatial resolution at the outermost domain, followed by 300 m resolution and an inner triangular nest of 150 m resolution. This inner nest was equivalent to a square grid of 100 m horizontal resolution, which is about one order of magnitude coarser than the observations by AISA Hawk. Simulations with finer horizontal resolution were not reasonable due to the high computational time. In the vertical direction, 150 height levels were simulated. In the ICON-LEM simulations the two-moment mixed-phase bulk microphysical parameterization by Seifert and Beheng (2006) was applied. It provided vertical profiles of liquid and ice mass mixing ratio  $r_w$ ,  $r_i$ , cloud droplets and ice crystal number concentration  $N_w$ ,  $N_i$ , air temperature  $T$ , and pressure  $p$ . The mass mixing ratio and the number concentration profiles take into consideration both, the non-precipitating (cloud water and cloud ice) and the precipitating (rain, snow, graupel and hail) hydrometeors. They have been used to convert the  $r_w$  and  $r_i$  into  $LWC$ , and  $IWC$ , as required by the radiative transfer model:

$$LWC(z) = r_w(z) \cdot \frac{p(z)}{R \cdot T(z)}, \quad IWC(z) = r_i(z) \cdot \frac{p(z)}{R \cdot T(z)} \quad (4)$$

with  $R = 287.06 \text{ J kg}^{-1} \text{ K}^{-1}$  the specific gas constant for dry air, and  $z$  the altitude. For the spherical liquid water droplets, vertical profiles of droplet effective radius are obtained by (Martin et al., 1994; Kostka et al., 2014):

$$r_{\text{eff,liquid}}(z) = \left[ \frac{3 \cdot r_w(z)}{4 \cdot \pi \cdot \rho_w \cdot N_w(z)} \right]^{1/3}, \quad (5)$$

where  $\rho_w$  is the density of the liquid water. For the non-spherical ice crystals, the median mass diameter  $D_{\text{m,ice}}$  of the particle size distribution (PSD) of cloud ice represented by the generalized  $\Gamma$ -distribution described by Seifert and Beheng (2006), used by ICON-LEM, is calculated as:

$$D_{\text{m,ice}}(z) = a \cdot \left[ \frac{r_i(z)}{N_i(z)} \right]^b, \quad (6)$$

with  $a=0.206 \cdot 10^{-6} \text{ m kg}^{-b}$  and  $b=0.302$ . The radiative properties of ice crystals were parameterized using the effective radius  $r_{\text{eff,ice}}$ . To convert the median particle size into radius  $r_{\text{eff,ice}}$ , the measurement-based relationship between  $D_{\text{m,ice}}$  and the effective diameter,  $D_{\text{eff,ice}}$ , of columnar ice crystals introduced by Baum et al. (2005) and Baum et al. (2014) was used.

### 3 Results of measurements and radiative transfer simulations

5 The ALOUD campaign was classified by Knudsen et al. (2018) into a cold (May 23 - May 29), a warm (May 30 - June 12) period, and a neutral period (June 13 - June 26). During the cold period, the Svalbard region was affected by a northerly cold air outbreak, which led to the development of low-level clouds over the warm open ocean. Over the Fram Strait, these clouds organized in a roll convective structure, forming typical cloud streets. During the warm period, a high pressure system south of Svalbard advected warm air from the south over the archipelago, leading to the development of a low-level, optically thick and homogeneous stratocumulus. Cold air outbreaks and warm air advections are phenomena often affecting the Arctic regions (Pithan et al., 2018; Sedlar and Tjernström, 2017; Woods et al., 2013; Kolstad et al., 2009; Fletcher et al., 2016). The occurrence of both situations during the ALOUD campaign make it an ideal testbed to contrast the characteristics of the clouds occurring under each situation. Two cloud cases observed on 25 May, during the cold air outbreak, and 2 June 2017, during the warm air advection, were analyzed in detail. Fig-Figure 2 displays the corresponding MODerate resolution Imaging Spectroradiometer (MODIS) true color images and shows the different clouds occurring showing the clouds on both days. The exact location of the observations is also indicated.

Figure 3 illustrates the combined measurements of MiRAC and AMALi for the one-minute sequence acquired over open ocean on the mentioned dates, for the two cloud cases. The combination of measurements is interpreted qualitatively to gain an insight into the clouds vertical structure. In both cases, the liquid cloud top is well visible identified by the strong backscatter of the lidar signal, defined as in Langenbach et al. (2019) and highly sensitive to liquid droplets. Whereas on 25 May the liquid layer is geometrically thicker, the lidar reaches the surface, which indicates a cloud optical thickness less than 3-4 (McGill et al., 2004). On 2 June, the lidar cannot penetrate the cloud. The stronger attenuation of the lidar signal, i.e., the rapid decrease in the lidar backscatter, hints at larger amounts of liquid than on 25 May. Contrastingly In contrast, the radar signal is dominated by larger particles, and significant higher radar reflectivity values can commonly indicate higher concentrations of ice crystals. The combination of the radar and lidar signals shows helps to identify differences in the vertical structure of both eases clouds. The cloud on 25 May, showing a high radar reflectivity, is contains very likely precipitating large ice crystals. In this case, some regions of the cloud present are characterized by a large radar reflectivity at cloud top, shown by the overlapping radar and lidar signals in Fig. 3a, which indicates hints at the presence of large particles in high cloud layers. Vertical separation between the signals of both instruments, such as occurring around 9:01:47, indicate regions where small liquid droplets dominate the cloud top, detected by the lidar but not by the radar. In these regions, the radar observes large particles, likely ice crystals, around 100 m below the cloud top which precipitate down to the surface. On 2 June (Fig. 3b), the radar reflectivity is in general weaker than on 25 May and shows a cloud that does not precipitate down to no evidence of precipitation reaching the surface. The weaker radar reflectivity may be attributed either to smaller ice crystals or to a reduced particle concentration. However,

the continuous overlap between the lidar and the radar signals ~~observed~~ in Fig. 3 indicates the presence of large particles right below the cloud top. These differences in the vertical structures of the two cloud cases need to be considered when interpreting the 2D horizontal fields of the slope phase index retrieved by AISA Hawk, which is most sensitive to the cloud top layer.

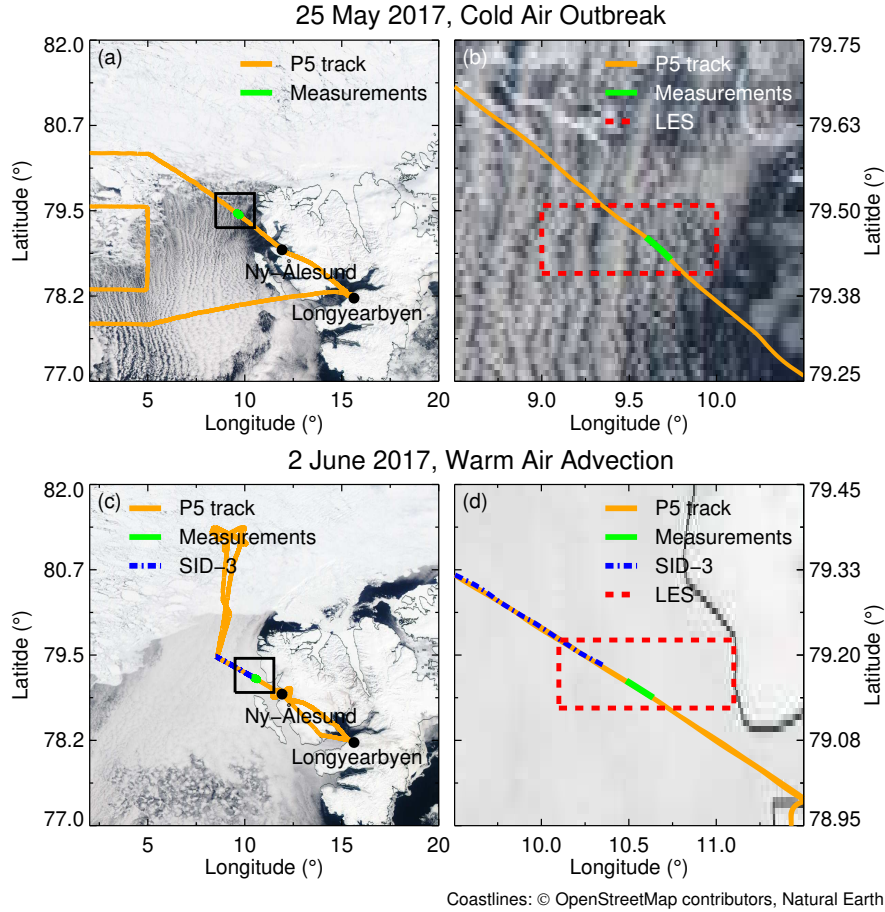


**Figure 2.** MODIS true color images from the NASA Worldview application (<https://worldview.earthdata.nasa.gov>) on 25 May 2017 (a) during a cold air outbreak and on 2 June 2017 (c) during a warm air advection. Zooms into the regions delimited by black squares are shown in (b) and (d). The measurements location (79.5° N, 9.5° E on 25 May and 79.2° N, 10.7° E on 2 June) is indicated by the green section of the flight track of Polar 5 (orange). The areas extracted from the LES are indicated by the dashed red rectangle. The dashed-dotted blue on 2 June line indicates the location of the ~~Small Ice Detector~~ (SID-3) measurements.

### 3.1 Cold air outbreak

- 5 Figure 4 presents a sequence of AISA Hawk measurements and retrieved horizontal fields of cloud properties ( $R_{1240}$ ,  $\mathcal{I}_s$ ,  $\tau$ ,  $\tau_{\text{eff}}$ , and  $LWP$ ) together with ~~their erresponding~~ corresponding histograms. They were observed during the cold air outbreak

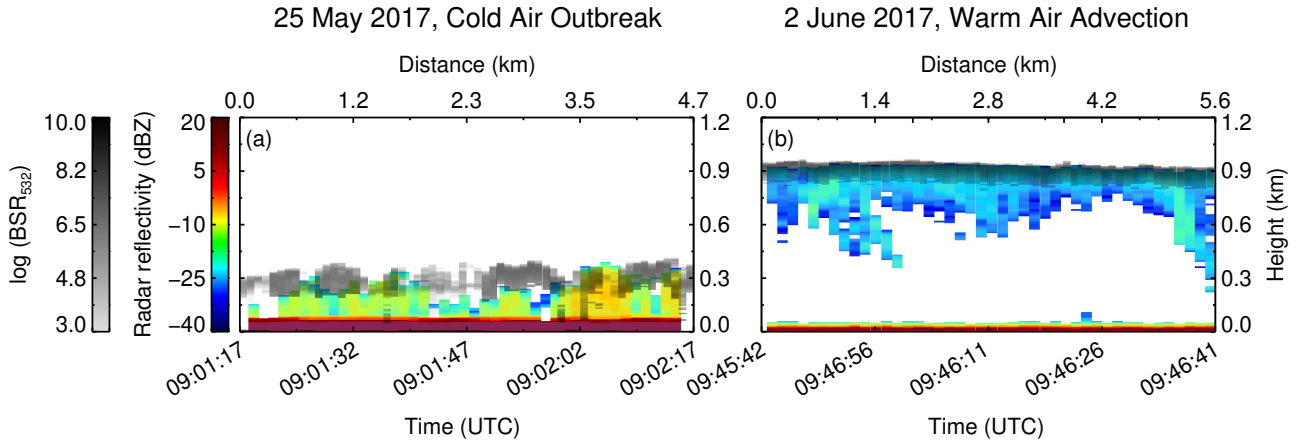


**Figure 3.** Combination of MiRAC radar reflectivity (color range between blue and red) and AMALi backscatter ratio (colors between white and black) as measured on 25 May 2017 during a cold air outbreak (a) and on 2 June 2017 during a warm air advection (b). AMALi’s lidar backscatter ratio is highly sensitive to the liquid droplets and shows the liquid top layer in both clouds. MiRAC’s radar reflectivity is dominated by larger particles and indicate regions with ice crystals. The radar signal below an altitude of 150 m is heavily influenced by ground clutter and cannot interpreted for cloud studies.

on 25 May 2017 in the flight section shown in Figs. 2a and 2b, ~~simultaneous to~~ simultaneously with the MiRAC and AMALi observations in Fig. 3a. ~~The statistics~~ Mean values and associated uncertainty of the cloud properties are summarized in Tab. 1. The measurements present one minute of data acquired at 9:01 UTC with a SZA of  $60.5^\circ$  at a flight altitude of 2.8 km. The average cloud top was located at 400 m above sea level. The observed cloud scene covers an area of  $1.411 \times 4.7 \text{ km}^2$  with an average pixel size of  $3.9 \times 2.6 \text{ m}^2$ . Figure 4a shows the cloud top reflectivity field at 1240 nm wavelength,  $R_{1240}$ , ~~with its histogram shown and a corresponding histogram~~ in Fig. 4b. Due to the broken ~~nature~~ character of the cloud field, a cloud mask has been applied prior to the retrieval of cloud properties. Based on radiative transfer simulations, a threshold of  $R_{1240} = 0.1$ , roughly corresponding to a  $LWP$  of  $2 \text{ g m}^{-2}$ , was chosen to discriminate between cloudy and cloud-free areas. Regions with  $R_{1240} < 0.1$  were classified as cloud-free and have been excluded ~~in the from~~ further analysis.

10 The slope phase index  $\mathcal{I}_s$ , presented in Figs. 4c and 4d, shows a maximum value of ~~11.5~~ 12.6, which is characteristic for pure liquid water clouds. This seems to disagree with the lidar and radar observations (Fig. 3), which indicated a mixed-phase ~~nature~~ cloud, and demonstrates the higher sensitivity of the phase index to the thermodynamic phase of the top most layer. Similarly, the  $LWP$  (Fig. 4i), calculated from  $\tau$  (Fig. 4e) and  $r_{\text{eff}}$  (Fig. 4g) using Eq. (3), increases towards the cloud core centers, as it is typical for pure liquid water clouds. These areas visually identify updraft regions where enhanced condensation

15 occurs due to adiabatic cooling (Gerber et al., 2005).

Although  $\mathcal{I}_s$  is always below the threshold of pure ice clouds, the cloud field presents significant small-scale variability that might be related to spatial changes in the thermodynamic phase distribution. To quantify if ~~the variability of regions of enhanced~~  $\mathcal{I}_s$  is related to the variability are correlated with areas of precipitating ice crystals, as observed by MiRAC, the

cloud edges were separated from the central cloud regions. All pixels below the 25th percentile of  $R_{1240}$  and of  $\mathcal{I}_s$  are defined as cloud edges. All other areas are considered to be cloud core center regions. The separated measurements were compared to 1D radiative transfer simulations adapted to the measurement situation. In Fig. 5, the ~~measurements are presented in a measured~~ slope phase index ~~reflectivity space is presented as a function of the cloud top reflectivity~~, together with simulations assuming pure-phase (either liquid or ice) clouds of known particle sizes and liquid/ice water paths. This sensitivity study shows the spread of  $\mathcal{I}_s$  as a function of the cloud thermodynamic phase, the cloud optical thickness (or  $LWP$ ,  $IWP$ ), and the cloud particle size ~~under the measurement conditions~~. An accurate phase classification cannot rely on a fixed  $\mathcal{I}_s$  threshold value and depends on the combined  $\mathcal{I}_s$  ~~and~~  $R_{1240}$  values. Fig. 5 reveals that the observed  $\mathcal{I}_s$  and  $R_{1240}$  range within simulated values covered by pure liquid water clouds. ~~Analyzing the~~ The spatio-temporal changes of the measurement (color code in Fig. 5) ~~indicates indicate~~ that a transition from cloud edge into cloud core follows lines with increasing  $LWP$  and slightly increasing particle sizes. This pattern can be explained by the dynamical and microphysical processes in cloud cores where ascending air condenses and cloud droplets grow with altitude leading to a higher  $LWP$ . Hence, the small-scale variability of  $\mathcal{I}_s$  observed on 25 May 2017 can be interpreted as the natural variability of the cloud top liquid layer. Compared to the radar observations, the passive reflectivity measurements are insensitive to the precipitating ice crystals.

**Table 1.** Average value and ~~standard deviation uncertainty~~ ( $\sigma\Delta$ ) of the cloud top properties derived from the measurements of AISA Hawk on 25 May and on 2 June. Independent estimations of the  $LWP$  range by the passive 89 GHz channel of MiRAC are also included.

	25 May 2017	2 June 2017
$z_{\text{top}}$ (m)	400	900
SZA ( $^\circ$ )	60.5	57.9
$\bar{R}_{1240} \pm \sigma_R \bar{R}_{1240} \pm \Delta \bar{R}_{1240}$	$0.23 \pm 0.08 \text{--} 0.01$	$0.65 \pm 0.04 \text{--} 0.03$
$\bar{\mathcal{I}}_s \pm \sigma_I \bar{\mathcal{I}}_s \pm \Delta \bar{\mathcal{I}}_s$	$7.47 \text{--} 3.36 \pm 1.3 \text{--} 0.04$	$20.42 \text{--} 0.3 \pm 1.3 \text{--} 1.0$
$\bar{\tau} \pm \sigma_\tau \bar{\tau} \pm \Delta \bar{\tau}$	$3.23 \text{--} 3.35 \pm 1.6 \text{--} 0.15$	$32.43 \text{--} 3.7 \pm 4.5 \text{--} 4.8$
$\bar{r}_{\text{eff}} \pm \sigma_r (\mu\bar{r}_{\text{eff}} \pm \Delta \bar{r}_{\text{eff}})$ ( $\mu\text{m}$ )	$4.7 \pm 1.2 \text{--} 1.5$	$12.9 \text{--} 12.5 \pm 2.7 \text{--} 3.5$
$\overline{LWP} \pm \sigma_{LWP} \overline{LWP} \pm \Delta \overline{LWP}$ ( $\text{g m}^{-2}$ )	$10.3 \pm 4.8 \text{--} 3.7$	$270.32 \text{--} 71 \pm 28.3 \text{--} 93$
$\Delta LWP_{\text{MiRAC}} \text{--} LWP_{\text{MiRAC}} \pm \Delta LWP_{\text{MiRAC}}$ ( $\text{g m}^{-2}$ )	$20 \pm 1 \text{--} 40 \pm 2$	$90 \pm 5 \text{--} 120 \pm 7$

## 15 3.2 Warm air advection

### 3.2.1 2D horizontal fields

A sequence of  $R_{1240}$  and retrieved cloud properties ( $\mathcal{I}_s$ ,  $\tau$ ,  $r_{\text{eff}}$ ,  $LWP$ ) observed in the ACLOUD warm period on 2 June 2017 is shown in Fig. 6 for the flight section of Fig. 3b. Table 1 ~~summarizes the statistics of the~~ presents the mean values and associated uncertainty of the presented cloud properties. The one-minute sequence starts at 9:45 UTC, when the SZA was of about  $57.9^\circ$ . The lidar observations indicated that the cloud top of the low-level stratocumulus was located at 900 m above sea level. Hence, for a flight altitude of 2.9 km, the field covers a cloud area of  $4.20 \text{--} 9 \times 5.6 \text{ km}^2$  with an average pixel size

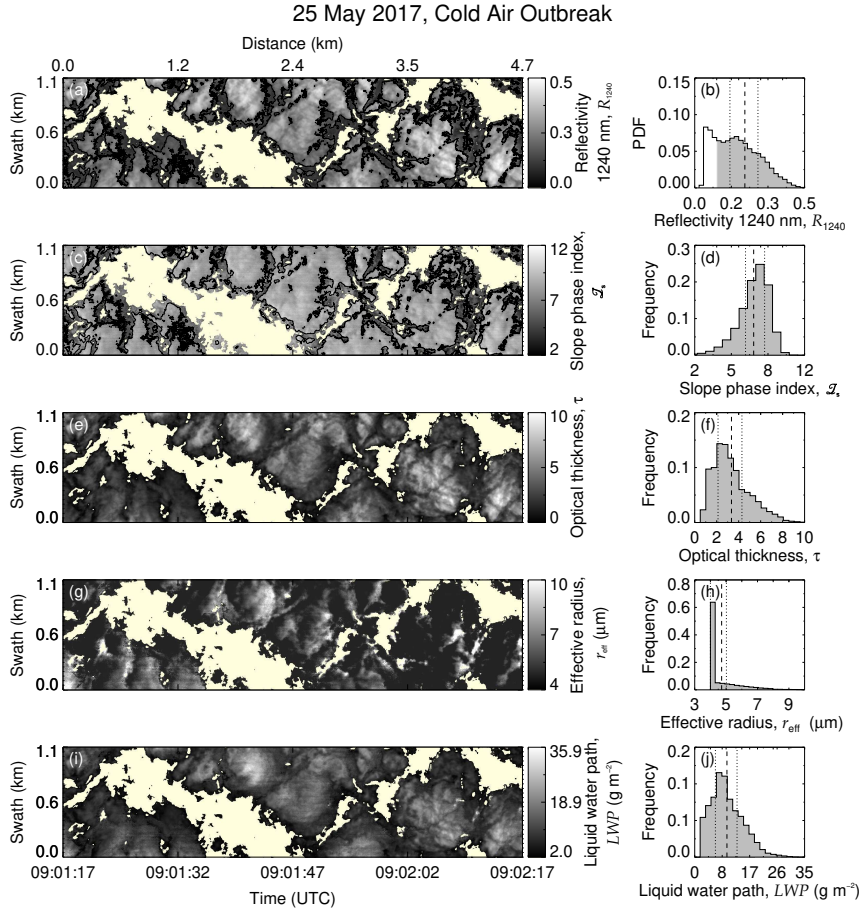


**Figure 4.** AISA Hawk measurement on 25 May 2017. Cloud top reflectivity (a), slope phase index (c), retrieved optical thickness (e), retrieved effective radius (g) and liquid water path (i). The overlaid contours in (a) and (c) separate the cloud central regions from the cloud edges. The frequency of occurrence histograms are displayed on the corresponding right-hand figures (b, d, f, h, j). Data classified as cloud free is shown by the non-colored histogram in (b). Dashed lines indicates the mean value of each field and the dotted lines show the corresponding 25th and 75th percentile.

of  $3.1 \times 4.7 \text{ m}^2$ . The cloud top reflectivity at 1240 nm wavelength, displayed in Fig. 6a ~~shows a more~~, shows a rather horizontally uniform cloud layer compared to the measurements collected on 25 May 2017 (Case I). The cloud mask ( $R_{1240} > 0.1$ ) reveals a 100 % cloud coverage for this scene. The slope phase index, presented in Fig. 6c, is higher compared to **Case I** the cloud case presented in Fig. 4 and ranges between ~~14.7 and 31.6~~ 14.9 and 36.5. Applying the common threshold of 20 would classify larger regions of the observed clouds as pure ice or mixed-phase. However, the  $LWP$  (Fig. 6i) shows significant variability over the entire cloud field, which may be related to the spatial distribution of the thermodynamic phase. The comparison of the relation between  $\mathcal{I}_s$  and  $R_{1240}$  with simulations assuming pure-phase clouds is shown in Fig. 7. The simulations

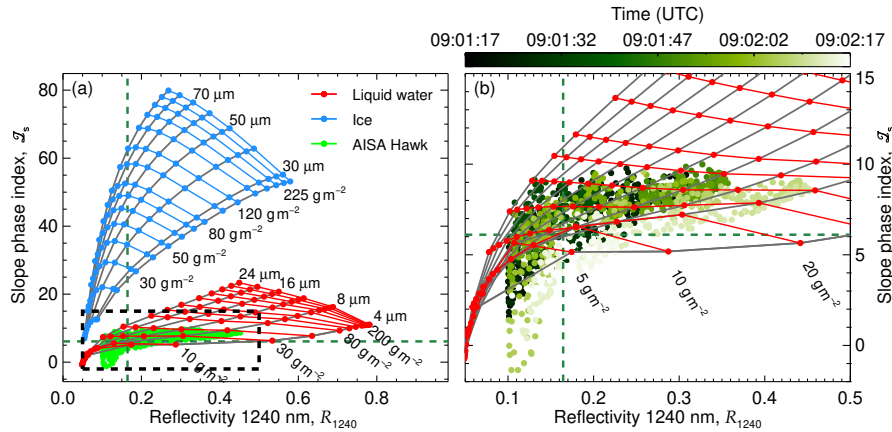


**Figure 5.** (a)  $\mathcal{I}_s$  measured on 25 May 2017 presented as a function of  $R_{1240}$  (green dots). The dashed lines indicate the 25th percentile of  $R_{1240}$  and  $\mathcal{I}_s$ . The two grids represent radiative transfer simulations for a range of pure liquid (red) and pure ice (blue) clouds. The liquid water clouds cover droplets with  $r_{\text{eff}}$  between 4 and 24  $\mu\text{m}$  and  $LWP$  between 1 and 250  $\text{g m}^{-2}$ . The ice clouds are simulated for columnar ice crystals with  $r_{\text{eff}}$  between 28 and 90  $\mu\text{m}$  and  $IWP$  between 1 and 250  $\text{g m}^{-2}$ . A SZA of 60.5° was considered. (b) Zoom of the area highlighted by a dashed rectangle in (a). Color-coded is the acquisition time of the measurements illustrating changes along the flight path.

reveal that the measurements do not fall in the range of the grid simulated for pure ice clouds, which would typically have higher values of slope phase index than observed. The measurements rather resemble the simulations of pure liquid water clouds. However, the field and histogram of  $LWP$  (Figs. 6i and 6j) show values in the range of 270  $\text{g m}^{-2}$  with 25 % percentile at 250  $\text{g m}^{-2}$ . Such high  $LWP$  values have rarely been observed in Arctic low-level clouds, which typically ~~do not~~ ranges between 30 and 50  $\text{g m}^{-2}$  and rarely exceed 100  $\text{g m}^{-2}$  (Shupe et al., 2005; de Boer et al., 2009). ~~The measurements~~ (Shupe et al., 2005; de Boer et al., 2009; Mioche et al., 2017; Nomokonova et al., 2019; Gierens et al., 2019). The measurements by the passive 89 GHz channel of the microwave radiometer of MiRAC were used to ~~estimte~~ estimate the  $LWP$  independently (see App. A-B for retrieval description and uncertainty assessment). The values between 90 and 120  $\text{g m}^{-2}$  ~~indicates~~ indicate that the  $LWP$  retrieval using the AISA Hawk measurements is strongly overestimated likely due to the presence of ice crystals close to cloud top (compare Fig. 3). This is supported by the rather high optical thickness and particle sizes retrieved from AISA Hawk measurements, shown in Figs. 6e-h. As the retrieval assumes liquid droplets, the presence of ice crystals, which are typically larger and strongly absorb radiation at 1625 nm, ~~did wavelength,~~ bias the retrieval of both quantities towards higher values (Riedi et al., 2010). The particle size distribution observed by the ~~Small Ice Detector (SID-3, Schnaiter et al., 2016)~~ SID-3 (Schnaiter and Järvinen, 2019b) deployed in Polar 6 between 9:25 and 9:35 UTC in the vicinity of the AISA Hawk ~~measurements (Fig. 2) revealed that, for the observed cloud, the particles at cloud top present effective radii in the range of 10  $\mu\text{m}$~~  (Schnaiter and Järvinen, 2019a). 75 % of the AISA Hawk measurements on 2 June retrieve an effective radii larger than this value (Figs. 6g and 6h). The small-scale variability of the cloud properties shows that the largest deviation of the retrieved  $r_{\text{eff}}$  and  $LWP$  respect the external measurements occurs in areas of low reflectivity (below the 25th percentile of  $R_{1240}$ ) and

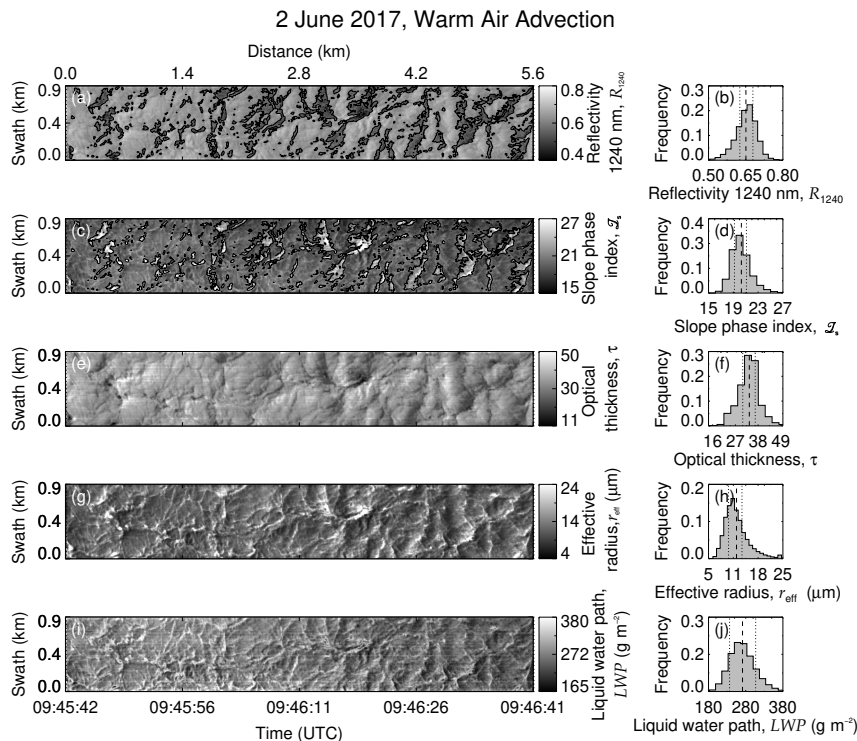


**Figure 6.** AISA Hawk measurement on 2 June 2017. Cloud top reflectivity (a), slope phase index (c), retrieved optical thickness (e), retrieved effective radius (g) and liquid water path (i). The overlaid contours in (a) and (c) separate the cloud central regions from the cloud edges. The frequency of occurrence histograms are displayed on the corresponding right-hand figures (b, d, f, h, j). The dashed line indicates the mean value and the dotted lines show its 25th and 75th percentile.

high slope phase index values (above the 75th percentile of  $\mathcal{I}_s$ ). These areas indicate cloud holes, where the vertical velocity is likely downwards and the condensation of liquid droplets is reduced, which increases the fraction of ice crystals. Although the theory predicts low values of  $LWP$  and  $r_{\text{eff}}$  in these regions (Gerber et al., 2005, 2013), the high ice fraction leads to the strong overestimation of  $LWP$  compared to the microwave retrieval. In contrast to the pattern observed on 25 May 2017, the higher ice fraction in the edges of the cloud holes causes the slope phase index to decrease with increasing cloud top reflectivity.

### 3.2.2 Impact of the vertical distribution of ice and water

We investigate whether the variability of  $\mathcal{I}_s$  on 2 June provides information on the vertical mixing structure of ice and liquid particles. Mixed-phase clouds commonly observed in the Arctic commonly consist of a single layer of supercooled liquid water droplets at cloud top, from which ice crystals precipitate (Mioche et al., 2015), which is in line with the radar/lidar observations presented in Fig. 3. Additionally, Ehrlich et al. (2009) found evidence of ice crystals near the cloud top. Based on these findings,  $\mathcal{I}_s$  of Horizontal inhomogeneities in the vertical distribution of the liquid water and ice occur in horizontal scales

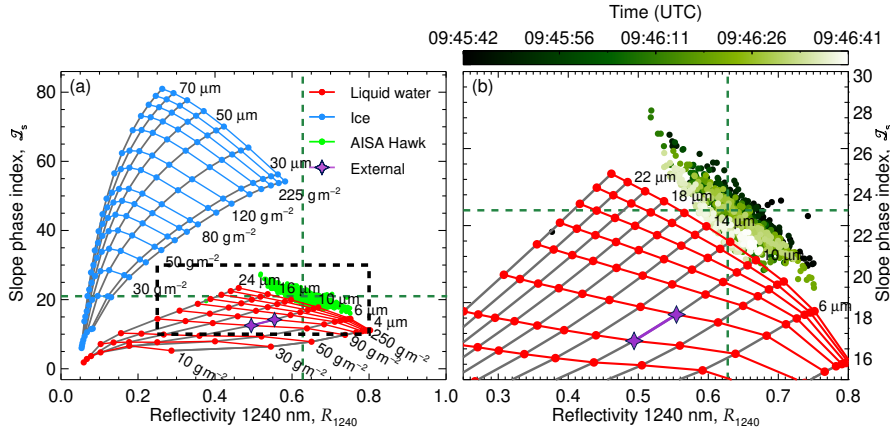


**Figure 7.** (a)  $\mathcal{I}_s$  measured on 2 June 2017 presented as a function of  $R_{1240}$  (green dots). The dashed lines indicate the 25th percentile of  $R_{1240}$  and the 75th percentile of  $\mathcal{I}_s$ . The two grids represent radiative transfer simulations for a range of pure liquid (red) and pure ice (blue) clouds. The liquid water clouds cover droplets with  $r_{\text{eff}}$  between 4 and 24  $\mu\text{m}$  and  $LWP$  between 1 and 250  $\text{g m}^{-2}$ . The ice clouds are simulated for columnar ice crystals with  $r_{\text{eff}}$  between 28 and 90  $\mu\text{m}$  and  $IWP$  between 1 and 250  $\text{g m}^{-2}$ . A SZA of 57.9° was considered. The purple stars shows the independent  $LWP$  range retrieved by the 89 GHz passive channel of MiRAC and the SID-3 in situ observation of particle size. (b) Zoom into the area highlighted by a dashed rectangle in (a). Color-coded is the acquisition time of measurements illustrating changes along the flight path.

of 10 m (Korolev and Isaac, 2006; Lawson et al., 2010) and are expected to relate to the small-scale structures (i.e., holes and domes) on the cloud top. Therefore, reproducing the observed trends of  $R_{1240}$  and  $\mathcal{I}_s$  with simulated mixed-phase clouds was simulated assuming three can provide information about the horizontal distribution of the cloud thermodynamic phase vertical structure. For this reason, the  $R_{1240}$  and  $\mathcal{I}_s$  observed on 2 June are compared with three different vertical mixing scenarios.

- 5 A two-layer cloud scenario with a layer of liquid water droplets at cloud top (750 - 900 m) and a cloud bottom layer (600 - 750 m) consisting of precipitating ice particles was assumed to represent the common vertical-mixing-type two-layers vertical thermodynamic phase distribution. In a second and third scenario, a vertically homogeneous mixture of ice and liquid particles was assumed in the cloud layer (600 - 900 m) to simulate, to represent the case when both liquid water and ice crystals are also present at cloud top. For both cases, the in the upper cloud top layer. The partitioning between ice and liquid droplets
- 10 was varied by changing the ice fraction, defined by

$$IF = \frac{IWP}{TWP} \cdot 100\%, \quad (7)$$

with the total water path defined as  $TWP = LWP + IWP$ . Pure liquid water clouds correspond to  $IF = 0\%$  and pure ice clouds to  $IF = 100\%$ . The slope phase index and the reflectivity of the mixed-phase cases depends both spectral cloud top

- 15 reflectivity depend on the  $r_{\text{eff}}$  of the considered ice and liquid particles and on the  $TWP$ . To inspect the spread of  $\mathcal{I}_s$  as a function of  $R_{1240}$  for mixed-phase cases with different  $IF$ , either the  $r_{\text{eff}}$  of the liquid and ice particles, or the  $TWP$  were kept

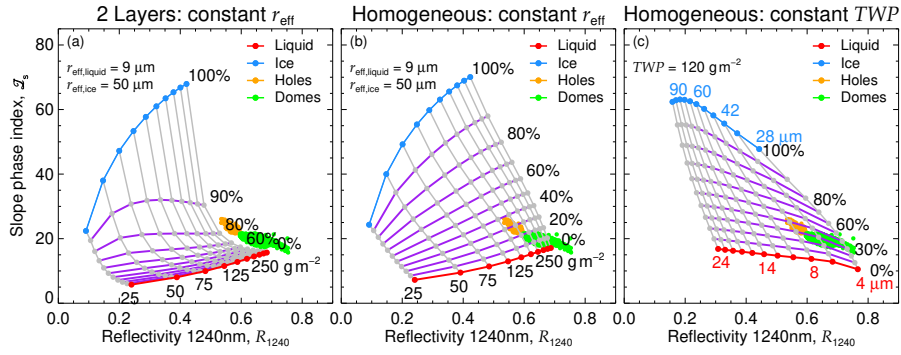


**Figure 8.** Comparison of  $\mathcal{I}_s$  measured on 2 June 2017 as a function of  $R_{1240}$  with three mixing scenarios of mixed-phase clouds. Observations in cloud holes are indicated by orange dots. Green dots represent measurements in cloud domes. Scenario (a) simulates a two layer cloud, while in scenarios (b) and (c) a homogeneously mixed cloud is assumed. Scenario (b) considers mixed-phase clouds of fixed particle sizes ( $r_{\text{eff,liquid}}$  of  $9 \mu\text{m}$  and  $r_{\text{eff,ice}}$  of  $50 \mu\text{m}$ ) and variable  $TWP$  between  $25$  and  $250 \text{ g m}^{-2}$ . The grey solid lines connect clouds of equal  $TWP$  and the solid purple lines, clouds of equal  $IF$  (indicated by the percentages). In scenario (c)  $TWP$  is fixed to  $120 \text{ g m}^{-2}$  and the particle sizes are varied. Here, purple lines connect clouds of equal ice fraction and the grey lines connect clouds considering equal particle sizes.

constant. The ~~first approach (constant approach using a constant value of  $r_{\text{eff}}$ )~~ was evaluated for the two-layer (Fig. 8a) and the ~~homogeneous mixing scenario vertically homogeneous mixing scenarios~~ (Fig. 8b), considering a fixed  $r_{\text{eff}}$  of  $9 \mu\text{m}$  for the liquid droplets and  $50 \mu\text{m}$  for the ice crystals. The  $TWP$  was varied between  $25 \text{ g m}^{-2}$  and  $250 \text{ g m}^{-2}$ . The fixed  $TWP$  approach was evaluated for the homogeneous mixing scenario (Fig. 8c). Here, the  $TWP$  was fixed to  $120 \text{ g m}^{-2}$ . In this case, the  $r_{\text{eff}}$  ~~range ranges~~ between  $4 \mu\text{m}$  and  $24 \mu\text{m}$  for liquid droplets and between  $28 \mu\text{m}$  and  $90 \mu\text{m}$  for ice crystals. The three scenarios show grids of  $\mathcal{I}_s$  where the increasing  $IF$  yields different patterns. The comparison with the measurements shows that only the homogeneously mixed scenarios (Figs. 8b and 8c) ~~may~~ reproduce the measured values of the slope phase index. In the two-layers scenario (Fig. 8a), the liquid water signature dominates  $\mathcal{I}_s$ , masking the presence of the cloud ice. These mixed-phase clouds need to be formed of at least  $IF = 70 \%$  to cause phase indices that effectively differ from those of pure liquid clouds. Additionally, the  $TWP$  required to match the observations exceeds the observed values. This indicates that a significant amount of ice near the cloud top is needed to explain the observed high values of  $\mathcal{I}_s$ .

The homogeneous ~~phase mixing~~ scenario presented on Fig. 8b could explain part of the observed values of the reflectivity and slope phase index. According to this scenario, the cloud holes (reflectivity below the 25th percentile of  $R_{1240}$ ) would show higher ice fractions (between  $20 \%$  and  $30\text{--}40 \%$ ) and higher  $\mathcal{I}_s$  than the cloud dome centers (reflectivity above the 25th percentile of  $R_{1240}$  and phase index below the 75th percentile of  $\mathcal{I}_s$ ), where  $IF$  is between  $0$  and  $20 \%$ . Figure 8c shows the alternative scenario where the  $TWP$  is fixed to  $120 \text{ g m}^{-2}$ . The simulated clouds cover most of the observed combinations of slope phase indices and reflectivities. In this scenario, the observed cloud would agree with mixed-phase clouds of fixed  $IF$  of about  $40 \%$ . In contrast to the scenario with fixed  $r_{\text{eff}}$ , this pattern indicates that the ice fraction in the cloud centers is similar to that in the cloud holes. The cloud domes centers consist of small droplets with effective radii between  $4 \mu\text{m}$  and  $6 \mu\text{m}$  and

small ice crystals with effective radii between  $28 \mu\text{m}$  and  $36 \mu\text{m}$ . Larger droplets, with  $r_{\text{eff}}$  between  $6 \mu\text{m}$  and  $8 \mu\text{m}$ , and ice crystals, with  $r_{\text{eff}}$  between  $36 \mu\text{m}$  and  $42 \mu\text{m}$  are found in the cloud holes. This pattern can be explained by a quick evaporation of small droplets in the cloud holes leading to a larger  $r_{\text{eff}}$ . Both idealized homogeneous mixing scenarios reproduce the observations. However, based on the AISA Hawk measurements of  $\mathcal{I}_s$  alone, it cannot be judged which scenario is more likely.

- 5 In reality, neither the particle sizes nor the  $TWP$  are horizontally fixed in a cloud field. A combination of both scenarios might be closest to reality. However, due to the large number of possible realizations (combinations of  $IWP$ ,  $LWP$ ,  $r_{\text{eff,ice}}$ ,  $r_{\text{eff,liquid}}$ ), it is impossible to fully resemble the observations.

#### 4 Large Eddy Simulations (Comparison of measurements and LES)

To characterize how more realistic vertical distributions of the thermodynamic phase impact the cloud top horizontal variability, the observed horizontal fields of  $\mathcal{I}_s$  were compared with results of simulations using the ICOSahedral Non-hydrostatic atmosphere model (ICON), operated in its Large Eddy Model (LEM) configuration (Heinze et al., 2017; Dipankar et al., 2015). The Comparing simulated cloud top reflectivities and phase index based on ICON-LEM is forced by initial and lateral boundary conditions from the European Centre for Medium-Range Weather Forecasts (ECMWF) Integrated Forecast System (IFS; Gregory et al., 2010). The simulations were performed in a one-way nested setup with a 600-m spatial resolution at the outermost domain, followed by 300-m resolution and an inner triangular nest of 150-m resolution. This inner nest is equivalent to a square grid of 100-m horizontal resolution, which is about an order of magnitude coarser than the observations by AISA Hawk. Simulations with finer horizontal resolution are not reasonable due to the high computational time. Two cloud fields with the measurements of AISA Hawk will help to evaluate the conclusions about the vertical structure of the cloud thermodynamic phase drawn in the previous section.

20 For the two cloud cases of 25 May and 2 June, two regions of  $21 \text{ km} \times 11 \text{ km}$  enclosing the corresponding aircraft measurements on 25 May and 2 June (Fig. 2) were selected. In the vertical direction, 150 height levels were simulated were simulated by ICON-LEM (Fig. 2). ICON-LEM uses the two-moment mixed-phase bulk microphysical parameterization by Seifert and Beheng (2006) and provided profiles of liquid and ice mixing ratio  $r_w$ ,  $r_i$ , cloud droplets and ice crystal number concentration  $N_w$ ,  $N_i$ , temperature  $T$ , and pressure  $p$ . The mixing ratio and the number concentration profiles take into consideration both the non-precipitating (cloud water and cloud ice) and the precipitating (rain, snow, graupel and hail) hydrometeors. They have been used to convert the  $r_w$  and  $r_i$  into  $LWC$ , and  $IWC$ , as required by the radiative transfer model:-

$$\underline{LWC(z) = r_w(z) \cdot \frac{p(z)}{R \cdot T(z)}, \quad IWC(z) = r_i(z) \cdot \frac{p(z)}{R \cdot T(z)}}$$

with  $R = 287.06 \text{ J kg}^{-1} \text{ K}^{-1}$  the specific gas constant for dry air. For the spherical liquid droplets, profiles of liquid effective radius are obtained by (Martin et al., 1994; Kostka et al., 2014):-

30 
$$\underline{r_{\text{eff,liquid}}(z) = \left[ \frac{3 \cdot r_w(z)}{4 \cdot \pi \cdot \rho_w \cdot N_w(z)} \right]^{1/3}},$$

where  $\rho_w$  is the density of the liquid water. For the non-spherical ice crystals, the median mass diameter  $D_{m,ice}$  of the particle size distribution (PSD) of cloud ice represented by the generalized  $\Gamma$ -distribution described by Seifert and Beheng (2006), used by ICON-LEM, is calculated as:-

$$D_{m,ice}(z) = a \cdot \left[ \frac{r_i(z)}{N_i(z)} \right]^b,$$

5 with  $a = 0.206 \cdot 10^{-6} \text{ m kg}^{-b}$  and  $b = 0.302$ . The radiative properties of ice crystals are parameterized using the effective radius  $r_{eff,ice}$ . To convert the median particle size into radius  $r_{eff,ice}$ , the measurement-based relationship between  $D_{m,ice}$  and the effective diameter,  $D_{eff,ice}$ , of columnar ice crystals shown by Baum et al. (2005) and Baum et al. (2014) was used. For the two cloud cases of 25 May and 2 June, the converted cloud The resulting cloud profiles are shown in Figs. 9a, 9d, 9c, and 9e-9e, and 9g. The profiles of ice fraction  $IF(z)$  shown in Figs. 9b and 9f are calculated, in correspondence to Eq. 7, by:

$$10 \quad IF(z) = \frac{IWC(z)}{LWC(z) + IWC(z)} \cdot 100\%. \quad (8)$$

On 25 May, the clouds simulated by ICON-LEM are located at higher altitudes than observed. However, the simulated profiles of  $LWC$ ,  $IWC$ , and  $IF$  agrees with confirm the vertical cloud structure indicated by the active remote sensing measurements (Fig. 3a), with both liquid and ice phases being present. The  $IWC$  reaches a maximum value of  $0.08 \text{ g m}^{-3}$  430 m below the  $0.12 \text{ g m}^{-3}$  maximum  $LWC$  at 900 m(9).

15 The cloud top reflectivities simulated by libRadtran on the basis of the clouds simulated by ICON-LEM have been used to derive cloud top reflectivities, which can be considered as synthetic measurements to calculate  $\mathcal{I}_s$ . These synthetic  $\mathcal{I}_s$  are compared to the observations of AISA Hawk using the relation of  $R_{1240}$  and  $\mathcal{I}_s$  introduced in (Figs. 5 and 7). To further test the sensitivity of  $R_{1240}$  and  $\mathcal{I}_s$  towards the vertical distribution of the cloud thermodynamic thermodynamic phase, additional synthetic cloud top reflectivities (firstly, neglecting the LES simulated IWC and therefore, hence considering pure liquid water clouds, and secondly, doubling the LES simulated IWC), were also simulated investigated. The comparisons with the AISA Hawk measurements is shown in Fig. 9d. The relation between  $R_{1240}$  and  $\mathcal{I}_s$  derived from the LES original  $LWC$  and  $IWC$  profiles shows that the liquid water dominated the cloud top layer, making its  $R_{1240}$  and  $\mathcal{I}_s$  indiscernible from those of pure liquid water clouds. This is almost identical to the AISA Hawk measurements (Fig. 9d). Only a few data points with higher  $\mathcal{I}_s$  range above the grid of pure liquid water clouds. These data mostly have low  $R_{1240}$  and can be linked to cloud edges with 25 lower  $LWP$  located outside the measurement area of AISA Hawk, where ice fractions are simulated to be higher than in the observations observed. Doubling the simulated IWC produced by ICON-LEM on 25 May (resulting in a maximum  $0.16 \text{ g m}^{-2}$  at 470 m) yielded a similar result: as for the original ICON-LEM originally simulated profiles, the  $R_{1240}$  and  $\mathcal{I}_s$  relation is for most LES pixels dominated by the higher liquid water concentration at cloud top and cannot be differenciaded differentiated from pure liquid water clouds. However, the enhanced  $IWC$  increases  $\mathcal{I}_s$  beyond values corresponding to pure liquid water clouds for a larger amount of cloud edge pixels than with the original LES IWC originally simulated by ICON-LEM.

30 On 2 June, ICON-LEM produces a maximum  $IWC$  of  $1.5 \cdot 10^{-4} \text{ g m}^{-3}$  located 170 m below the maximum  $0.37 \text{ g m}^{-3}$   $LWC$  at 530 m. As for 25 May, the vertical profiles of  $IWC$  and  $LWC$  agree with the active remote sensing measurements (Fig. 3)bb),

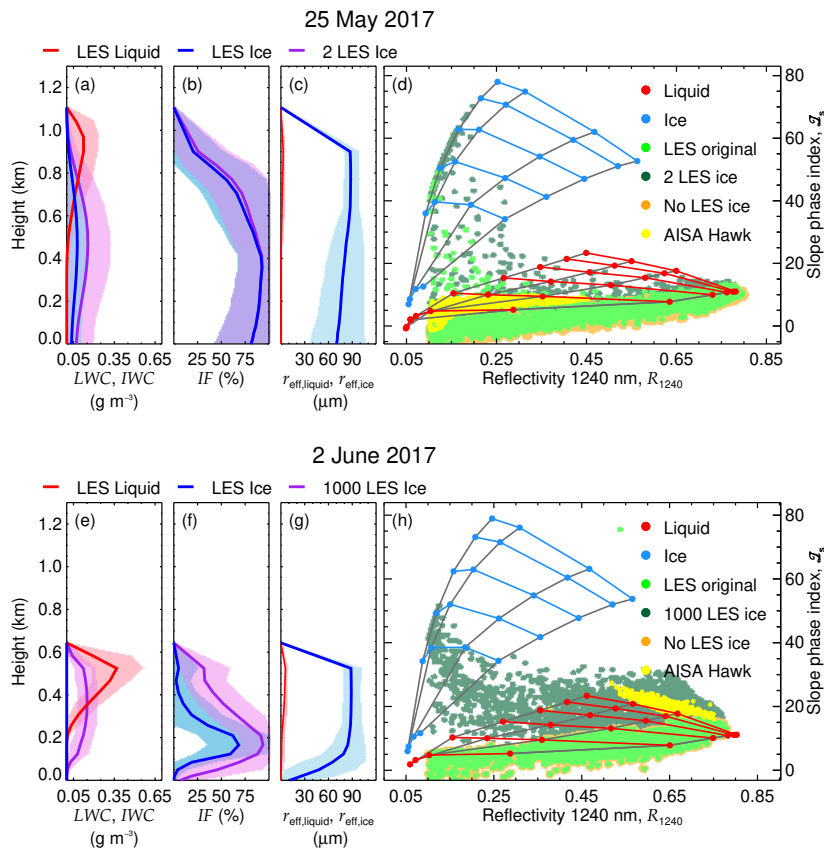


**Figure 9.** Mean profiles of liquid and ice water content, ice fraction and effective radius (**a**, **b**, and **c** for 25 May 2017 and **e**, **f**, and **g** for 2 June 2017, respectively). The shaded areas indicate the standard deviation of the considered distribution. The simulated  $R_{1240}$  and  $\mathcal{I}_s$  corresponding to the original LES profiles, as well as simulations neglecting the  $IWC$  (‘No LES ice’) and modifying it (‘2 LES ice’ for 25 May and ‘1000 LES ice’ for 2 June), are compared with  $R_{1240}$  and  $\mathcal{I}_s$  of pure phase clouds and the AISA Hawk measurements in (**d**) (25 May) and (**h**) (2 June).

indicating the presence of both liquid and ice. However, as demonstrated by Fig. 9h, the original  $IWC$  ~~produced-simulated~~ by ICON-LEM is too low to effectively impact  $R_{1240}$  and  $\mathcal{I}_s$ , which follow the pattern of pure liquid water clouds and did not reproduce the AISA Hawk observations. This difference suggests that the ICON-LEM underestimates the concentration of ice for the cloud on 2 June 2017. In a test case, the  $IWC$  was increased by a factor of 1000 ~~so-that-it-reached-a-maximum~~ ~~value-(maximum value of  $1.5 \times 10^{-4} \text{ g m}^{-3}$  at 360 m)~~ in the same order of magnitude than the maximum  $LWC$ . For this hypothetical cloud field, the radiative transfer simulations reproduced the observed values of  $\mathcal{I}_s$ , which deviate from the pure liquid case. However, the results of the ICON-LEM simulations show many data points with  $R_{1240}$  way below the observations ( $R_{1240} < 0.45$ ). This indicates that the cloud field produced by the LES, covering a larger area than the observations, presents

significant cloud gaps (low  $TWP$ ), which were ~~not observed by AISA Hawk~~ located outside the AISA Hawk measurement region. For the manipulated cloud, these cloud parts show a significant increase of  $\mathcal{I}_s$  with decreasing  $R_{1240}$ , which can be attributed to cloud edges similar to the cold air outbreak case of 25 May.

## 5 Impact of spatial resolution

5 The horizontal resolutions of the ICON-LEM (100 m) and the airborne observations (10 m) differ by about one order of magnitude. Additionally, satellite-borne imaging spectrometers commonly used to derive global distributions of cloud properties typically do not reach a spatial resolution as high as the AISA Hawk measurements. For instance, the Advanced Very High Resolution Radiometer (AVHRR), the MODerate resolution Imaging Spectroradiometer (MODIS), and the Hyperion imaging spectrometer have resolutions of 1000 m, 500 m, and 2530 m pixel sizes, respectively (Kaur and Ganju, 2008; Li et al., 2003; 10 Thompson et al., 2018). This raises the question of how much of the observed variability of  $\mathcal{I}_s$  is lost by horizontal averaging. ~~In order to assess the information lost by the coarser resolutions~~ To assess this question, the AISA Hawk observations of the two cloud cases were averaged for larger pixel sizes. Figures 10 and 11 show a ~~1000900~~ 1000900 m  $\times$  ~~1000900~~ 1000900 m subsection of the original fields of  $R_{1240}$  and  $\mathcal{I}_s$  projected for pixel sizes of 2530 m (Hyperion), 10090 m ( $\sim$ ICON-LEM), 500450 m ( $\sim$ MODIS), and ~~1000900~~ 1000900 m ( $\sim$ AVHRR). The relationship between  $\mathcal{I}_s$  and  $R_{1240}$  of the complete fields is illustrated in Figs. 10c, 10f, 10i, 10l, 15 and 10o for 25 May 2017 and in Figs. 11c, 11f, 11i, 11l, and 11o for 2 June 2017. The statistics of  $R_{1240}$  and  $\mathcal{I}_s$  corresponding to the considered pixel sizes for both days are presented in Tab. 2.

**Table 2.**  $R_{1240}$  and  $\mathcal{I}_s$  dependence upon the sensor resolution.

		25 May 2017				2 June 2017			
		Min.	Max.	25th percentile	75th percentile	Min.	Max.	25th percentile	25th percentile
$R_{1240}$	Original	0.10	<del>0.47</del> <u>0.50</u>	0.16	0.28	<del>0.46</del> <u>0.18</u>	<del>0.76</del> <u>0.83</u>	0.63	<del>0.67</del> <u>0.68</u>
	<u>2530</u> m	0.10	<del>0.45</del> <u>0.48</u>	0.16	0.28	<del>0.47</del> <u>0.45</u>	<del>0.74</del> <u>0.76</u>	0.63	<del>0.67</del> <u>0.68</u>
	<u>10090</u> m	0.10	<del>0.40</del> <u>0.42</u>	0.16	<del>0.27</del> <u>0.28</u>	<del>0.53</del> <u>0.51</u>	<del>0.71</del> <u>0.72</u>	0.63	0.67
	<u>500450</u> m	<del>0.14</del> <u>0.13</u>	<del>0.32</del> <u>0.33</u>	0.17	0.22	<del>0.62</del> <u>0.63</u>	<del>0.66</del> <u>0.67</u>	0.64	0.66
	<u>1000900</u> m	<del>0.15</del> <u>0.14</u>	0.23	0.15	<del>0.23</del> <u>0.20</u>	0.64	0.66	0.64	<del>0.66</del> <u>0.65</u>
$\mathcal{I}_s$	Original	<del>0.44</del> <u>2.12</u>	<del>10.8</del> <u>11.7</u>	<del>6.75</del> <u>6.54</u>	<del>8.25</del> <u>8.29</u>	<del>16.3</del> <u>15.0</u>	<del>31.3</del> <u>36.3</u>	<del>19.5</del> <u>19.1</u>	21.0
	<u>2530</u> m	<del>2.09</del> <u>0.07</u>	<del>9.80</del> <u>9.90</u>	<del>6.76</del> <u>6.60</u>	<del>8.22</del> <u>8.23</u>	<del>17.0</del> <u>16.5</u>	<del>27.8</del> <u>29.8</u>	<del>19.6</del> <u>19.3</u>	20.9
	<u>10090</u> m	<del>4.84</del> <u>3.45</u>	9.43	<del>6.83</del> <u>6.62</u>	<del>8.13</del> <u>8.08</u>	<del>18.0</del> <u>17.7</u>	<del>24.0</del> <u>25.0</u>	<del>19.8</del> <u>19.5</u>	20.7
	<u>500450</u> m	<del>6.74</del> <u>5.54</u>	<del>8.14</del> <u>8.15</u>	<del>7.10</del> <u>6.94</u>	<del>7.96</del> <u>7.67</u>	<del>19.5</del> <u>19.0</u>	20.9	<del>20.1</del> <u>19.3</u>	<del>20.5</del> <u>20.4</u>
	<u>1000900</u> m	<del>6.88</del> <u>6.60</u>	<del>7.91</del> <u>7.71</u>	<del>7.21</del> <u>6.77</u>	<del>7.91</del> <u>7.13</u>	<u>19.1</u>	19.9	<del>20.5</del> <u>19.5</u>	<del>20.1</del> <u>20.4</u> <u>19.7</u>

The ~~subsequent~~ smoothing of the cloud scene with increasing pixel size erases the fine spatial structure of the cloud top, which remains only visible for 25 m pixel size. For the cloud case of 25 May 2017, the horizontal averaging mainly impacts the observed cloud geometry. The decreasing contrast between the cloudy and cloud-free pixel changes the cloud mask and

eventually causes the loss of the cloud broken nature observed by AISA Hawk. The original range of variability of  $R_{1240}$  between 0.10 and ~~0.47-0.50~~ decreases to the range between ~~0.15-0.14~~ and 0.23 at ~~1000~~900 m. The original range of  $\mathcal{I}_s$  between ~~0.44 and 10.81-2.12 and 11.7~~ is reduced to the range from ~~6.88 to 7.91~~~~6.60 to 7.71~~, but always indicates a cloud that is dominated by the liquid layer at cloud top. For the cloud on 2 June 2017 (Fig. 11), the averaging cannot affect the 100 % cloud cover. However, the variability of  $R_{1240}$  becomes significantly reduced for larger pixel sizes (from the original variability between ~~0.46 and 0.76-0.18 and 0.83~~ to a variability at ~~1000~~900 m between 0.64 and 0.66) as no large-scale cloud structures are present. Similarly, the variability of  $\mathcal{I}_s$  diminishes for observations with coarser spatial resolution from the original range between ~~16.3 and 31.3 to 19.9 and 20.5-15.0 and 36.3 to 19.1 and 19.9~~ for pixels of ~~1000~~900 m). A coarser resolution removes the contrast between cloud holes, which are typically characterized by the presence of ice crystals (high  $\mathcal{I}_s$ ) and the cloud domes, where liquid droplets dominate (lower  $\mathcal{I}_s$ ). For satellite observations with pixel sizes larger than ~~100~~90 m, this prevents from characterizing and interpreting the change of cloud phase in the small scale cloud structure and ~~therefore-~~ therefore, conceals the information about the vertical distribution of the thermodynamic phase contained in the cloud top variability. High resolved imaging spectrometer measurements such as the Hyperion and the ICON-LEM, with pixels below 100 m are still able to resolve part of the natural horizontal variability.

## 15 6 Conclusions

Based on airborne active and passive remote sensing conducted by a passive imaging spectrometer and vertically resolving ~~techniques-instruments~~, such as lidar and radar, the horizontal and vertical structure of the thermodynamic phase in Arctic mixed-phase ~~clouds-cloud cases~~ was characterized for two example clouds observed during a cold air outbreak and a warm air intrusion event. While the spectral imaging was used to identify the structure of the horizontal distribution of the cloud ice ~~in-at~~ scales down to 10 m, the combined radar and lidar observations revealed the general vertical thermodynamic phase distribution of the clouds.

The two ~~analyzed~~ cloud cases were observed over open ocean close to Spitzbergen during the ALOUD campaign. The cloud scene sampled on 25 May 2017 ~~was linked to evolved within~~ a cold air outbreak, whereas a cloud that had formed in a warm air advection event was sampled on 2 June 2017. For both cloud cases, the combined radar and lidar observations indicated the mixed-phase character of the clouds ~~with liquid-~~ with liquid water droplets in the cloud top layer and ice crystals ~~in lower cloud layers below~~. While the lidar ~~could~~ penetrated the strongly reflecting liquid cloud layer on 25 May ~~farther, seeing the surface at some instances, the quick-~~ partly until the surface, the strong extinction of the lidar signal close to the cloud top observed on 2 June indicates higher liquid water amounts. The vertical structure of the radar backscatter also differs between both days, with reflectivities reaching the ground on 25 May typical for light snow precipitation. These different cloud vertical structures influenced the ability to detect the ~~cloud-ice~~ by the solar imaging-imaging spectrometer observations of AISA Hawk ~~-evaluated~~ using the slope phase index  $\mathcal{I}_s$ . On 25 May,  $\mathcal{I}_s$  is dominated by the liquid water ~~in-contained at~~ the cloud top layer, which leads to a ~~misclassification-misclassification~~ as a pure liquid water cloud. The small-scale variability of  $\mathcal{I}_s$  observed on 25 May relates mostly to the variability of the liquid cloud layers. On 2 June, AISA Hawk measured higher  $\mathcal{I}_s$ , which requires

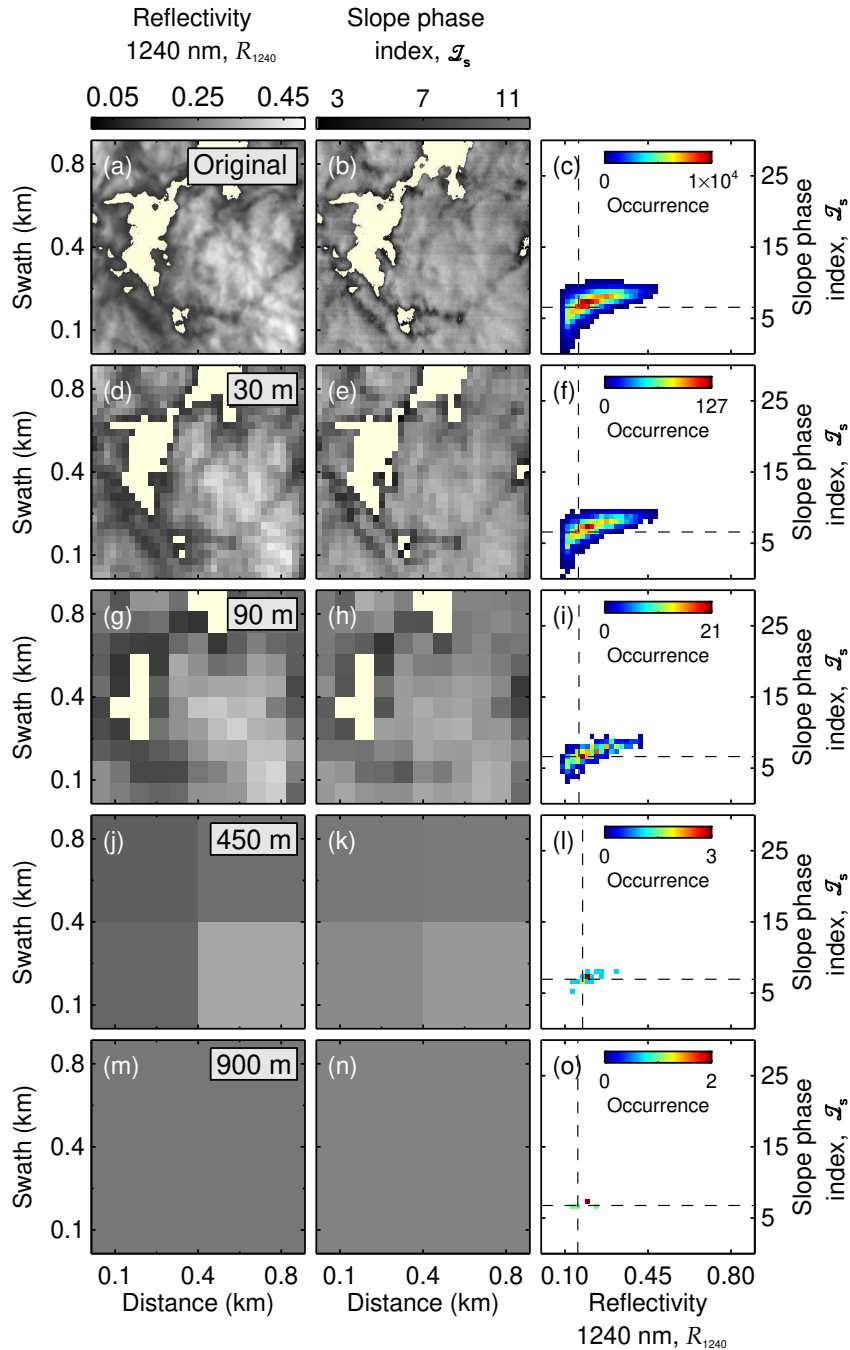


**Figure 10.** Slope phase index - 1240 nm reflectivity relationship for 5 different pixel sizes (original AISA Hawk resolution, 2530 m, 10090 m, 500450 m, and 1000900 m). (a), (d), and (g) show a 1 km  $\times$  1 km subsection of  $R_{1240}$  measured on 25 May 2017 as seen by the five different resolutions; (b), (e), and (h), the corresponding 1 km  $\times$  1 km  $\mathcal{I}_s$ ; and (c), (f) and (i) present the scatter between both magnitudes for the complete 1 km  $\times$  4 km field. The dashed lines indicate the 25th percentile of  $R_{1240}$  and  $\mathcal{I}_s$  for each resolution.

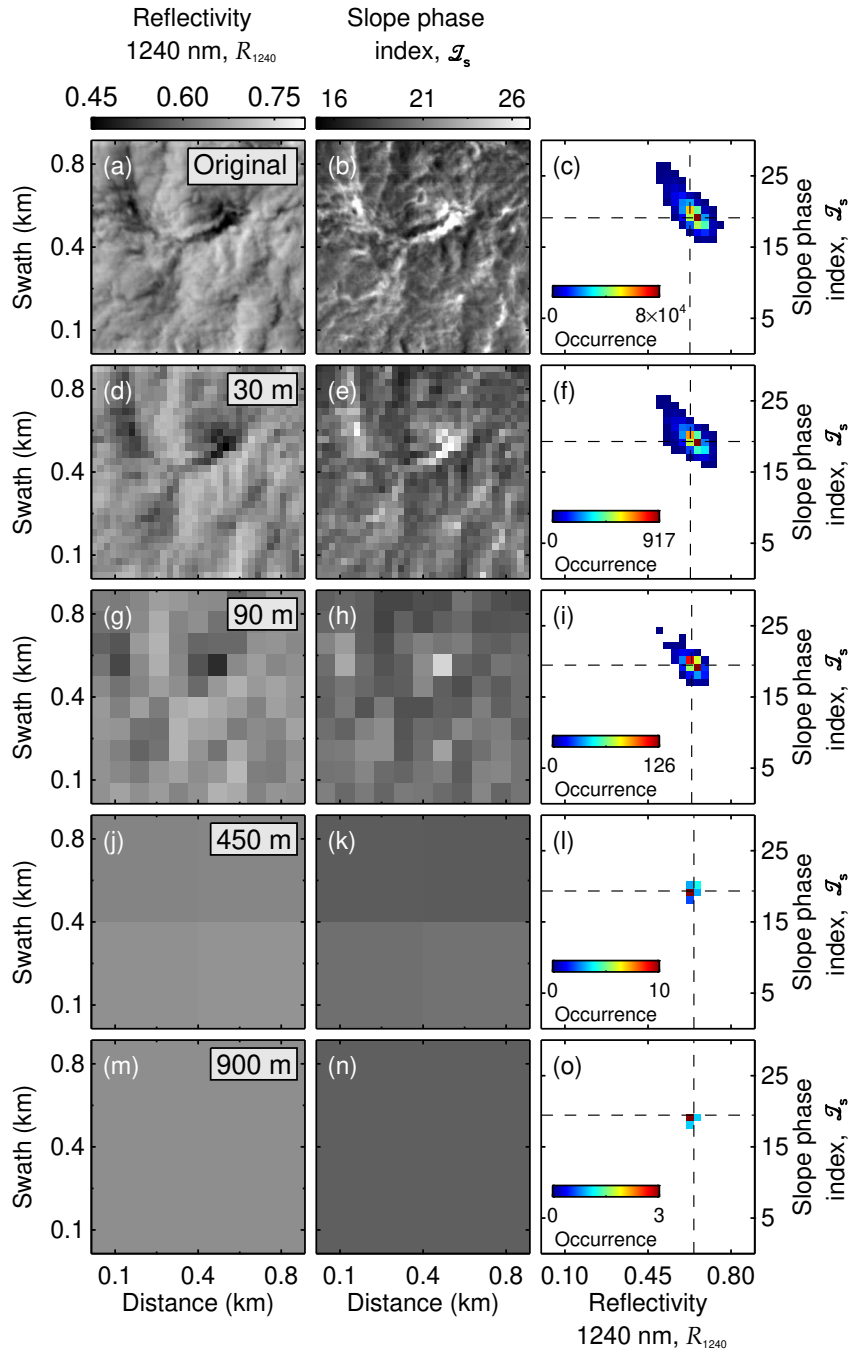


**Figure 11.** Slope phase index - 1240 nm reflectivity relationship for 5 different pixel sizes (original AISA Hawk resolution, 2530 m, 10090 m, 500450 m, and 1000900 m). (a), (d), and (g) show a 1 km  $\times$  1 km subsection of  $R_{1240}$  measured on 2 June 2017 as seen by the five different resolutions; (b), (e) and (h), the corresponding 1 km  $\times$  1 km  $\mathcal{I}_s$ ; and (c), (f) and (i) present the scatter between both magnitudes for the complete 1 km  $\times$  4 km field. The dashed lines indicate the 25th percentile of  $R_{1240}$  and  $\mathcal{I}_s$  for each resolution.

hints at the presence of ice crystals in higher cloud layers ~~to be explained~~. Additionally, the *LWP*, retrieved ~~on the assumption of~~ ~~by assuming~~ pure liquid clouds, shows ~~unrealistic-unrealistically~~ high values compared to the observations by MiRAC, which supports this conclusion. The high values of  $\mathcal{I}_s$  and the large retrieval bias of *LWP* are observed close to areas of low cloud reflectivity (cloud holes). The comparison of both cloud cases ~~demonstrates that a~~ ~~highlights the limitations of passive remote~~ ~~sensing alone to identify layered mixed-phase structures if the ice is not sufficiently close to the cloud top. In particular in these~~ ~~cases, the~~ combination of active and passive remote sensing is ~~needed-crucial~~ to fully characterize the horizontal and vertical distribution of ice and liquid ~~water~~ particles in mixed-phase clouds.

The ~~variability-highly resolved horizontal distribution~~ of  $\mathcal{I}_s$  observed on 2 June was ~~analysed-analyzed~~ using radiative transfer simulations assuming different mixing scenarios of ~~the ice and the ice and~~ liquid water content. Two homogeneous ~~mixing scenarios, either keeping the TWP or the particle sizes fixed when changing the ice fraction, did reproduce the observed pattern of variability. However, based on the AISA Hawk measurements of  $\mathcal{I}_s$  alone, it cannot be judged which scenario is closer to reality. To consider modeled~~ ~~mixing-phase-mixing~~ scenarios of *IWP*, *LWP*,  $r_{\text{eff,ice}}$ ,  $r_{\text{eff,liquid}}$  and the vertical cloud structure, the ICON-LEM was applied. The microphysical profiles simulated by ICON-LEM ~~agree-with-roughly represent major features~~ ~~of~~ the vertical profiles obtained by MiRAC and AMALi for both cloud cases. To compare with the AISA Hawk measurements, ~~radiative transfer simulations of the cloud top were performed on the basis of the ICON-LEM thermodynamic phase profiles. For both cases,~~ the variability of  $\mathcal{I}_s$  calculated from the simulations is represented by pure liquid water clouds. Enhancing the *IWC* simulated by ICON-LEM indicates that, whereas on 25 May this behavior is due to the liquid-water-dominated cloud top layer, on 2 June, the simulated concentration of ice crystals is underestimated. In a test case where the ~~IWC-IWC~~ was enhanced 1000 times, the simulated cloud central regions showed a comparable structure as observed by AISA Hawk. Additionally, the ~~area simulated by ICON-LEM produced significant cloud gaps not present in the smaller cloud section observed by AISA Hawk. Similarly to 25 May, the cloud gaps present high values of  $\mathcal{I}_s$ . The comparison of the simulated  $\mathcal{I}_s$ - $R_{1240}$  patterns with measured ones can~~ ~~in-turn~~ be used used to assess the performance of ICON-LEM, which reproduces the vertical structure of the two observed cloud cases, but produces too little ice on 2 June. Nevertheless, to fully exploit the measurements-model synergy, synthetic radar and lidar measurements should be simulated based on ICON-LEM, taking as well into consideration ~~the ice habit~~ ~~observed-observed~~ by in-situ measurements.

The grid size of ICON-LEM (100 m) is sufficient to resolve the small-scale structure of mixed-phase clouds and to produce different patterns of  $\mathcal{I}_s$  giving indication on the vertical distribution of the cloud thermodynamic phase. A sensitivity study reducing the horizontal resolution of the passive remote sensing observations illustrated that pixel sizes below 100 m, such as provided by the Hyperion imager spectrometer or airborne spectral imagers, are required to resolve the horizontal distribution ~~of ice and liquid water in Arctic mixed-phase clouds. However, common satellite sensors such as MODIS or AVHRR are not able to capture the small-scale~~ ~~variability-distribution~~ of  $\mathcal{I}_s$ .

*Data availability.* The AISA Hawk (Ruiz-Donoso et al., 2019), SMART (Jäkel et al., 2019), MiRAC (Kliesch and Mech, 2019) and AMALi (Neuber et al., 2019) data, acquired during the ACloud campaign, are publicly available on PANGAEA. All other data used and produced in this study are available upon request from the corresponding authors.

## Appendix A: Analysis of 3D effects in the AISA Hawk measurements

- 5 The spatially highly-resolved radiance fields measured by AISA Hawk are affected by 3D radiative effects caused by the three-dimensional nature of the cloud top. Specifically, a) horizontal photon transport occurs between neighboring pixels, smoothing the measurements, and b) cloud top structures cast shadows on the image.

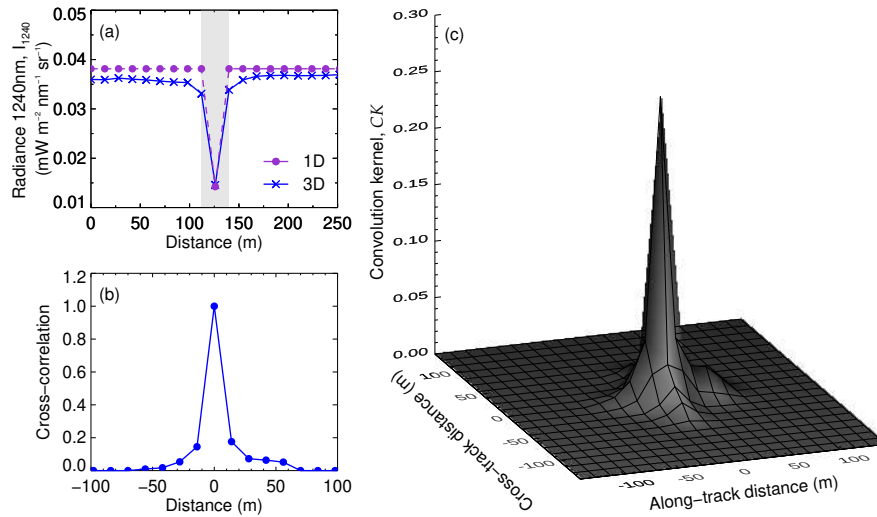


**Figure A1.** (a) Comparison of the nadir reflected radiance at 1240 nm by a stratiform cloud deck simulated with 1D and 3D radiative transfer simulations. The cloud contains a 15 m region of pure ice (shaded) embedded between two pure liquid water regions (non-shaded). (b) Cross-correlation between the 1D and the 3D cloud top radiance illustrating the extent of the horizontal photon transport. (c) Normalized convolution kernel based on the cross-correlation of the 1D and 3D simulations and different sun-sensor geometries.

In order to correct the smoothing due to horizontal photon transport, the horizontal sensitivity of each case study was estimated comparing 3D and 1D simulations of the cloud top reflected radiance. The 3D simulations of an idealized cloud field were performed with the Monte Carlo Atmospheric Radiative Transfer Simulator (MCARaTS, Wang et al., 2012) and the 1D simulations were performed with libRadtran. The cloud field considers a liquid water stratiform deck with a  $LWP$  similar to the observations (i.e.  $30 \text{ g m}^{-2}$  and  $100 \text{ g m}^{-2}$ , respectively), a typical  $r_{\text{eff}}$  of  $10 \mu\text{m}$  and solar zenith angle (SZA) of  $60^\circ$  and  $57^\circ$ , respectively. A pure ice region of 15 m width, with  $r_{\text{eff}}$  of  $60 \mu\text{m}$  and a  $IWP$  similar to the  $LWP$ , was embedded in the liquid deck. The change of cloud phase in general leads to a reduction of the cloud top radiance in the ice phase area. The 3D and 1D simulations of the  $100 \text{ g m}^{-2}$  case are presented in Fig. A1a. Whereas the 1D simulated radiance stays constant in

the liquid water region and decreases sharply within the ice stripe, the horizontal photon transport smooths the transition from the liquid to the ice region in the 3D radiance. The cross-correlation between both simulations, shown in Fig. A1b, provides an estimation of the horizontal displacement of the photons in the 3D simulation, which is effective within distances of about 100 m. The combination of cross-correlation functions calculated for different solar azimuth angles, SAA, and different sensor viewing angles (therefore accounting for different sun-sensor geometries) yields the three dimensional normalized convolution kernel  $CK$  presented in Fig. A1c. The simulations with  $LWP$  of  $30 \text{ g m}^{-2}$  (not shown here) yield a similar result. The derived  $CK$  accounts only for the mean photon transport of each field and does not consider local inhomogeneities. Similar to Zinner et al. (2006), in order to avoid overcompensating the horizontal photon transport, the iterative Richardson-Lucy deconvolution algorithm (Richardson, 1972; Lucy, 1974) was applied. After each iteration, the calculated radiance takes the form,

$$I_{n+1} = \left[ \left( \frac{I}{I_n \otimes CK} \right) \otimes CK \right], \quad (\text{A1})$$

where  $I$  is the radiance observed by AISA Hawk,  $I_n$  is the radiance obtained after the  $n^{\text{th}}$  iteration, and  $\otimes$  is the convolution operator. Based on the convergence of  $|I_{n+1} - I_n|/I_n$ , a number of 4 iterations was found to sufficiently increase the sharpness of the measured radiance fields.

However, the second 3D radiative effect, caused by the shadows casted by the cloud top geometry, cannot be easily corrected. Highly spatially resolved measurements of the cloud top geometry would be necessary for correcting self-shading artifacts. Therefore, 3D radiative transfer simulations are used to estimate this 3D radiative effect and analyze whether the observed correlation between  $R_{1240}$ ,  $\mathcal{I}_s$ , and  $LWP$  are caused by shadows or by inhomogeneous distributions of the cloud thermodynamic phase. Figure A2 presents 3D simulations of two idealized stratiform cloud decks with a constant  $TWP$  of  $100 \text{ g m}^{-2}$ .

Figure A2a represents a liquid water cloud with an inhomogenous cloud top height (50 m lower cloud top in the center of the cloud field). For a SZA of  $57^\circ$ , similar to the measurement on 2 June, the dip on the cloud top casts a shadow that gets imprinted on  $R_{1240}$  (A2c),  $\mathcal{I}_s$  (A2e) and the retrieved  $LWP$  (A2g). Whereas in the shaded region  $R_{1240}$  decreases on average by 35 % with respect to the non-shaded region,  $\mathcal{I}_s$  increases on average by 20 %. These opposite effects result in an almost constant  $LWP$ , which does not show a signature of the cloud dip.

Figure A2b shows a pure liquid water cloud with a constant cloud top height and an embedded mixed-phase region of 150 m horizontal extent. The  $TWP$  is kept always constant at  $100 \text{ g m}^{-2}$  (i.e. the pure phase region considers a  $LWP$  of  $100 \text{ g m}^{-2}$ ; the mixed-phase region considers a  $LWP$  of  $60 \text{ g m}^{-2}$  and a  $IWP$  of  $40 \text{ g m}^{-2}$ ). The liquid water droplets have an  $r_{\text{eff}}$  of  $10 \mu\text{m}$  and the ice crystals have an  $r_{\text{eff}}$  of  $60 \mu\text{m}$ . The inhomogeneous phase distribution obviously biases the retrieved cloud top properties and the calculated phase index. In this case,  $R_{1240}$  (A2d) decreases by 34 % in the mixed-phase region compared to the pure-phase region,  $\mathcal{I}_s$  increases by 58 %. However, contrasting the shaded case, the presence of ice crystals lead to a significant increase of  $LWP$  by 36 %.

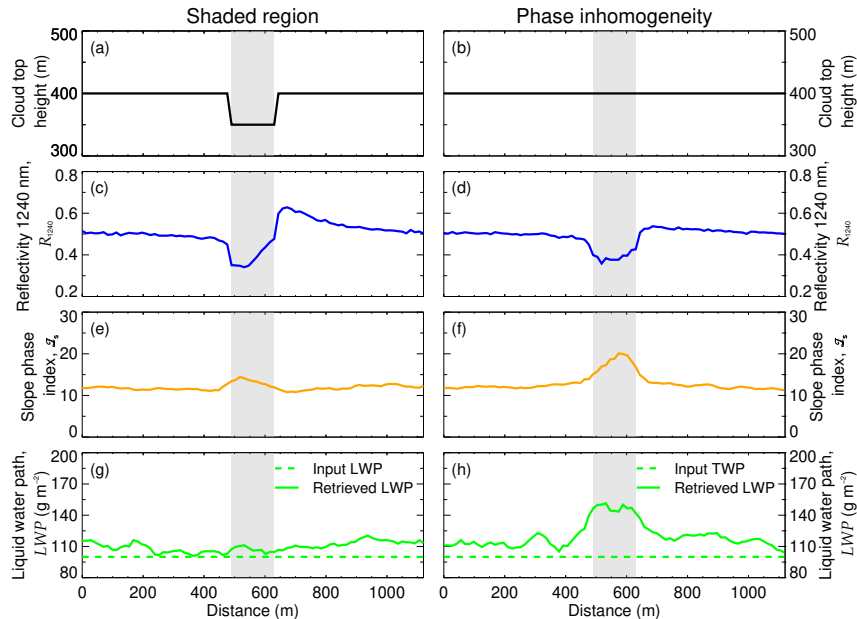


**Figure A2.** Cloud top properties of a shaded region (a, c, e, g) compared to a region with a different thermodynamic phase composition (b, d, f, h). The shaded areas indicates the artifact affected areas

Therefore, the combination of  $R_{1240}$ ,  $I_s$  and  $LWP$  is crucial to interpret the observations of AISA Hawk. Only a simultaneous increase in  $I_s$  and  $LWP$  when  $R_{1240}$  decreases is indicative of mixed-phase regions. Although we cannot completely discard shading artifacts on the 2 June case study, the observed increment of  $I_s$  and  $LWP$  in regions of low  $R_{1240}$  agrees with the simulations in Figs. A2d, A2f and A2h and support the hypothesis of mixed-phase on this day.

## 5 Appendix B: $LWP$ retrieval based on passive microwaver radiometer measurements

Measurements by the 89 GHz passive channel of the Microwave Radiometer for Arctic Clouds (MiRAC, Mech et al., 2019) were used to estimate the liquid water path ( $LWP$ ) for the two case studies. Brightness temperatures (TB) were measured under a tilted angle of  $25^\circ$  with respect to nadir backwards with 1 s integration time. At this frequency, TB depends on the surface emission, dependent in turn on the sea surface temperature (SST) and wind speed, and on atmospheric contributions by atmospheric gases and cloud liquid. Cloud ice does not contribute to the signal and only strong snowfall could lead to TB reduction by scattering, i.e.  $500 \text{ g m}^{-2}$  snowfall correspond to about 1-2 K reduction. On short time scales – such as the two minute long flight tracks – variations are mainly caused by cloud variability. Therefore, a simplified algorithm exploiting the relative change of TB compared to a base state was developed.

For each of the two cases, the closest dropsonde was used to calculate TB as a function of  $LWP$ , assuming a cloud between 500 and 100 m above sea level. Within these microwave radiative transfer simulations, the wind speed was taken from the

lowest available dropsonde level ( $5 \text{ m s}^{-1}$  on 25 May and  $7.7 \text{ m s}^{-1}$  on 2 June) and the SST (275 K) from climatological data. Liquid water emission leads to an increase in TB above the radiatively cold ocean. When subtracting the clear sky TB ( $\text{TB}_0$ ), the resulting  $\Delta\text{TB}$  can be well approximated by a third order regression with an uncertainty of ca.  $1 \text{ g m}^{-2}$  in *LWP*. Due to the different wind speed and moisture conditions of the two cases, uncertainties of about  $5 \text{ g m}^{-2}$  ( $12 \text{ g m}^{-2}$ ) at  $100 \text{ g m}^{-2}$  (200  $\text{g m}^{-2}$ ) *LWP* occur.

The clear sky  $\text{TB}_0$  needs to be derived before applying the simple regression algorithm to calculate  $\Delta\text{TB}$ . For this purpose, we searched for the minimum TB in both cases and checked whether the lidar signal was low. This is to some degree subjectively and difficult due to the high cloud presence (see Figs. 4 and 6). In fact, for 2 June a profile approximately 5 min later was chosen. With our best estimates of  $\text{TB}_0$  (180 K on 25 May and 186 K on 2 June) for each one second measurement, *LWP* could be derived, yielding a range between 20 and  $40 \text{ g m}^{-2}$  for 25 May and 90 to  $120 \text{ g m}^{-2}$  for 2 June.

While the approach to derive *LWP* from a single frequency is rather simple, it also presents advantages (for example, absolute calibration errors are avoided due to the use of difference values). Changes in SST, wind speed and moisture content of the two one-minute time periods are thought to play a minor role and estimated to be below 10%. The highest uncertainty is thought to stem from the determination of the clear sky  $\text{TB}_0$ . However, the maximum uncertainty is estimated to be about  $30 \text{ g m}^{-2}$  and thus, the 2 June case clearly (i) has a higher *LWP* than the 25 May case and (ii) has a lower *LWP* than the one estimated by AISA Hawk (Tab. 1). In the future, additional measurements from higher MiRAC frequency channels and lidar information will be exploited to retrieve a higher accuracy *LWP* product.

*Author contributions.* MW, AE and SW designed the experimental basis of this study. ERD, MS and EJ acquired the measurements of AISA Hawk and SMART. ERD selected the case studies, processed and analyzed the measurements of AISA Hawk, performed the 1D radiative transfer simulations, and drafted the manuscript. EJ processed the measurements of SMART and performed the 3D radiative transfer simulations. MM and RN acquired the measurements of MiRAC and AMALi. SC, MM, BSK, LLK and RN processed and analyzed the measurements of MiRAC and AMALi. VS performed the ICON-LEM simulations. AE, MS and MW provided technical guidance. All authors contributed to the editing of the manuscript and to the discussion and interpretation of the results.

*Competing interests.* The authors declare that they have no conflict of interests.

*Acknowledgements.* We gratefully acknowledge the funding by the Deutsche Forschungsgemeinschaft (DFG, German Research Foundation) – Projektnummer 268020496 – TRR 172, within the Transregional Collaborative Research Center “Arctic Amplification: Climate Relevant Atmospheric and SurfaCe Processes, and Feedback Mechanisms (AC)<sup>3</sup>”.

## References

- Baum, B., Yang, P., Heymsfield, A. J., Bansemer, A., Cole, B. H., Merrelli, A., Schmitt, C., and Wang, C.: Ice cloud single/scattering property models with the full phase matrix at wavelengths from 0.2 to 100  $\mu\text{m}$ , *J. Quant. Spectrosc. Radiat. Transfer*, 146, 123–139, <https://doi.org/10.1016/j.jqsrt.2014.02.029>, 2014.
- 5 Baum, B. A., Heymsfield, A. J., Yang, P., and Bedka, S. T.: Bulk scattering properties for the remote sensing of ice clouds. Part I: Microphysical data and models, *J. Appl. Meteor.*, 44, 1885–1895, <https://doi.org/10.1175/JAM2308.1>, 2005.
- Bierwirth, E., Ehrlich, A., Wendisch, M., Gayet, J.-F., Gourbeyre, C., Dupuy, R., Herber, A., Neuber, R., and Lampert, A.: Optical thickness and effective radius of Arctic boundary-layer clouds retrieved from airborne nadir and imaging spectrometry, *Atmos. Meas. Tech.*, 6, 1189–1200, <https://doi.org/10.5194/amt-6-1189-2013>, 2013.
- 10 Chylek, P. and Borel, C.: Mixed phase cloud water/ice structure from high spatial resolution satellite data, *Geophys. Res. Lett.*, 31, <https://doi.org/10.1029/2004GL020428>, 2004.
- de Boer, G., Eloranta, E. W., and Shupe, M. D.: Arctic mixed-phase stratiform cloud properties from multiple years of surface-based measurements at two high-latitude locations, *J. Atmos. Sci.*, 66, 2874–2887, <https://doi.org/10.1175/2009JAS3029.1>, 2009.
- Dipankar, A., Stevens, B., Heinze, R., Moseley, C., Zängl, G., Giorgetta, M., and Brdar, S.: Large eddy simulation using the general circulation model ICON, *J. Adv. Model. Earth Sy.*, 7, 963–986, <https://doi.org/10.1002/2015MS000431>, 2015.
- 15 Egerer, U., Gottschalk, M., Siebert, H., Ehrlich, A., and Wendisch, M.: The new BELUGA setup for collocated turbulence and radiation measurements using a tethered balloon: first applications in the cloudy Arctic boundary layer, *Atmos. Meas. Tech.*, 12, 4019–4038, <https://doi.org/10.5194/amt-12-4019-2019>, 2019.
- Ehrlich, A.: The impact of ice crystals on radiative forcing and remote sensing of Arctic boundary-layer mixed-phase clouds, Ph.D. thesis, Johannes Gutenberg University Mainz, Germany, 2009.
- 20 Ehrlich, A., Bierwirth, E., Wendisch, M., Gayet, J.-F., Mioche, G., Lampert, A., and Heintzenberg, J.: Cloud phase Identification of Arctic boundary-layer clouds from airborne spectral reflection measurements: test of three approaches, *Atmos. Chem. Phys.*, <https://doi.org/10.5194/acp-8-7493-2008>, 2008a.
- Ehrlich, A., Wendisch, M., Bierwirth, E., Herber, A., and Schwarzenböck, A.: Ice crystal shape effects on solar radiative properties of Arctic mixed-phase clouds - Dependence on microphysical properties, *Atmos. Res.*, 88, 266–276, 2008b.
- 25 Ehrlich, A., Wendisch, M., Bierwirth, E., Gayet, J.-F., Mioche, G., Lampert, A., and Mayer, B.: Evidence of ice crystals at cloud top of Arctic boundary-layer mixed-phase clouds derived from airborne remote sensing, *Atmos. Chem. Phys.*, 9, 9401–9416, <https://doi.org/10.5194/acp-9-9401-2009>, 2009.
- Ehrlich, A., Wendisch, M., Lüpkes, C., Buschmann, M., Bozem, H., Chechin, D., Clemen, H.-C., Dupuy, R., Eppers, O., Hartmann, J., Herber, A., Jäkel, E., Järvinen, E., Jourdan, O., Kästner, U., Kliesch, L.-L., Köllner, F., Mech, M., Mertes, S., Neuber, R., Ruiz-Donoso, E., Schnaiter, M., Schneider, J., Stapf, J., and Zanatta, M.: A comprehensive in situ and remote sensing data set from the Arctic CLOUD Observations Using airborne measurements during polar Day (ACLOUD) campaign, *Earth Syst. Sci. Data Discus.*, 2019, 1–42, <https://doi.org/10.5194/essd-2019-96>, 2019.
- 30 Emde, C., Buras-Schnell, R., Kylling, A., Mayer, B. and Gasteiger, J., Hamann, U., Kylling, J., Richter, B., Pause, C., Downing, T., and Bugliaro, L.: The libRadtran software package for radiative transfer calculations (version 2.0.1), *Geosci. Model Dev.*, <https://doi.org/10.5194/gmd-9-1647-2016>, 2016.
- 35

- Field, P. R., Hogan, R. J., Brown, P. R. A., Illingworth, A. J., Choullarton, T. W., Kaye, P. H., Hirst, E., and Greenaway, R.: Simultaneous radar and aircraft observations of mixed-phase cloud at the 100 m scale, *Q. J. Royal Meteorol. Soc.*, 130, 1877–1904, <https://doi.org/10.1256/qj.03.102>, 2004.
- Fletcher, J., Mason, S., and Jakob, C.: The Climatology, Meteorology, and Boundary Layer Structure of Marine Cold Air Outbreaks in Both Hemispheres, *J. Climate*, 29, 1999–2014, <https://doi.org/10.1175/JCLI-D-15-0268.1>, 2016.
- Gerber, H., Frick, G., Malinowski, S. P., Brenguier, J.-L., and Burnet, F.: Holes and Entrainment in Stratocumulus, *J. Atmos. Sci.*, 62, 443–459, <https://doi.org/10.1175/JAS-3399.1>, 2005.
- Gerber, H., Frick, G., Malinowski, S. P., Jonsson, H., Khelif, D., and Krueger, S. K.: Entrainment rates and microphysics in POST stratocumulus, *Journal of Geophysical Research: Atmospheres*, 118, 12,094–12,109, <https://doi.org/10.1002/jgrd.50878>, 2013.
- 10 Gierens, R., Kneifel, S., Shupe, M. D., Ebell, K., Maturilli, M., and Löhnert, U.: Low-level mixed-phase clouds in a complex Arctic environment, *Atmos. Chem. Phys. Discuss.*, 2019, 1–37, <https://doi.org/10.5194/acp-2019-610>, 2019.
- Gregory, D., Morcrette, J.-J., Jakob, C., Beljaars, A. C. M., and Stockdale, T.: Revision of convection, radiation and cloud schemes in the ECMWF integrated forecasting system, *Q. J. Royal Meteorol. Soc.*, 126, 1685–1710, <https://doi.org/10.1002/qj.49712656607>, 2010.
- Heinze, R., Dipankar, A., Henken, C. C., Moseley, C., Sourdeval, O., Trömel, S., Xie, X., Adamidis, P., Ament, F., Baars, H., Barthlott, C., Behrendt, A., Blahak, U., Bley, S., Brdar, S., Brueck, M., Crewell, S., Deneke, H., Girolamo, P. D., Evaristo, R., Fischer, J., Frank, C., Friederichs, P., Göcke, T., Gorges, K., Hande, L., Hanke, M., Hansen, A., Hege, H., Hoose, C., Jahns, T., Kalthoff, N., Klocke, D., Kneifel, S., Knippertz, P., Kuhn, A., Laar, T. v., Macke, A., Maurer, V., Mayer, B., Meyer, C. I., Muppa, S. K., Neggers, R. A. J., Orlandi, E., Pantillon, F., Pospichal, B., Röber, N., Scheck, L., Seifert, A., Seifert, P., Senf, F., Siligam, P., Simmer, C., Steinke, S., Stevens, B., Wapler, K., Weniger, M., Wulfmeyer, V., Zängl, G., Zhang, D., and Quaas, J.: Large-eddy simulations over Germany using ICON: a comprehensive evaluation, *Q. J. Royal Met. Soc.*, 143, 69–100, <https://doi.org/10.1002/qj.2947>, 2017.
- 20 Hogan, R. J. and O’Conner, E.: Facilitating cloud radar and lidar algorithms: the Cloudnet Instrument Synergy/Target Categorization Product, Dept. of Meteorol. Univ of Reading, UK, <http://www.met.reading.ac.uk/~swrhgnrj/publications/categorization.pdf>, 2004.
- Horváth, A., Seethala, C., and Deneke, H.: View angle dependence of MODIS liquid water path retrievals in warm oceanic clouds, *J. Geophys. Res. Atmos.*, 119, 8304–8328, <https://doi.org/10.1002/2013JD021355>, 2014.
- 25 Jäkel, E., Walther, J., and Wendisch, M.: Thermodynamic phase retrieval of convective clouds: impact of sensor viewing geometry and vertical distribution of cloud properties, *Atmos. Meas. Tech.*, 6, 539–547, <https://doi.org/10.5194/amt-6-539-2013>, 2013.
- Jäkel, E., Ehrlich, A., Schäfer, M., and Wendisch, M.: Aircraft measurements of spectral solar up- and downward irradiances in the Arctic during the ALOUD campaign 2017, <https://doi.org/10.1594/PANGAEA.899177>, 2019.
- Kalesse, H., de Boer, G., Solomon, A., Oue, M., Ahlgrimm, M., Zhang, D., Shupe, M. D., Luke, E., and Protat, A.: Understanding Rapid Changes in Phase Partitioning between Cloud Liquid and Ice in Stratiform Mixed-Phase Clouds: An Arctic Case Study, *Mon. Wea. Rev.*, 144, 4805–4826, <https://doi.org/10.1175/MWR-D-16-0155.1>, 2016.
- 30 Kaur, R. and Ganju, A.: Cloud classification in NOAA AVHRR imageries using spectral and textural features, *Journal of the Indian Society of Remote Sensing*, 36, 167–174, <https://doi.org/10.1007/s12524-008-0017-z>, 2008.
- Klein, S. A., McCoy, R. B., Morrison, H., Ackerman, A. S., Avramov, A., de Boer, G., Chen, M., Cole, J. N. S., Del Genio, A. D., Falk, M., Foster, M. J., Fridlind, A., Golaz, J.-C., Hashino, T., Harrington, J. Y., Hoose, C., Khairoutdinov, M. F., Larson, V. E., Liu, X., Luo, Y., McFarquhar, G. M., Menon, S., Neggers, R. A. J., Park, S., Poellot, M. R., Schmidt, J. M., Sednev, I., Shipway, B. J., Shupe, M. D., Spangenberg, D. A., Sud, Y. C., Turner, D. D., Veron, D. E., von Salzen, K., Walker, G. K., Wang, Z., Wolf, A. B., Xie, S., Xu, K.-M.,

- Yang, F., and Zhang, G.: Intercomparison of model simulations of mixed-phase clouds observed during the ARM Mixed-Phase Arctic Cloud Experiment. I: Single-layer cloud, *Q. J. Royal Meteorol. Soc.*, 135, 979–1002, <https://doi.org/10.1002/qj.416>, 2009.
- Kliesch, L.-L. and Mech, M.: Airborne radar reflectivity and brightness temperature measurements with POLAR 5 during ALOUD in May and June 2017, <https://doi.org/10.1594/PANGAEA.899565>, 2019.
- 5 Knudsen, E. M., Heinold, B., Dahlke, S., Bozem, H., Crewell, S., Gorodetskaya, I. V., Heygster, G., Kunkel, D., Maturilli, M., Mech, M., Viceto, C., Rinke, A., Schmithüsen, H., Ehrlich, A., Macke, A., Lüpkes, C., and Wendisch, M.: Meteorological conditions during the ALOUD/PASCAL field campaign near Svalbard in early summer 2017, *Atmos. Chem. Phys.*, 18, 17995–18022, <https://doi.org/10.5194/acp-18-17995-2018>, 2018.
- Kokhanovsky, A.: Optical properties of terrestrial clouds, *Earth-Sci. Rev.*, 64, 189 – 241, [https://doi.org/10.1016/S0012-8252\(03\)00042-4](https://doi.org/10.1016/S0012-8252(03)00042-4),  
10 2004.
- Kollias, P., Miller, M. A., Luke, E. P., Johnson, K. L., Clothiaux, E. E., Moran, K. P., Widener, K. B., and Albrecht, B. A.: The Atmospheric Radiation Measurement Program Cloud Profiling Radars: Second-Generation Sampling Strategies, Processing, and Cloud Data Products, *Journal of Atmospheric and Oceanic Technology*, 24, 1199–1214, <https://doi.org/10.1175/JTECH2033.1>, 2007.
- Kolstad, E. W., Bracegirdle, T. J., and Seierstad, I. A.: Marine cold-air outbreaks in the North Atlantic: temporal distribution and associations  
15 with large-scale atmospheric circulation, *Climate Dyn.*, 33, 187–197, 2009.
- Korolev, A.: Limitations of the Wegener-Bergeron-Findeisen mechanism in the evolution of mixed-phase clouds, *J. Atmos. Sci.*, 64, 3372–3375, <https://doi.org/10.1175/JAS4035.1>, 2007.
- Korolev, A. and Field, P. R.: The effect of dynamics on mixed-phase clouds: Theoretical considerations, *J. Atmos. Sci.*, 65, 66–86, <https://doi.org/10.1175/2007JAS2355.1>, 2008.
- 20 Korolev, A. and Isaac, G. A.: Relative humidity in liquid, mixed-phase, and ice clouds, *J. Atmos. Sci.*, 63, 2865–2880, <https://doi.org/10.1175/JAS3784.1>, 2006.
- Korolev, A., Mcfarquhar, G., R. Field, P., Franklin, C., Lawson, P., Wang, Z., Williams, E., J. Abel, S., Axisa, D., Borrmann, S., Crosier, J., Fugal, J., Krämer, M., Lohmann, U., Schlenzcek, O., and Wendisch, M.: Ice Formation and Evolution in Clouds and Precipitation: Measurement and Modeling Challenges. Chapter 5: Mixed-phase clouds: progress and challenges., *AMS Meteorological Monographs*,  
25 pp. 5.1–5.50, 2017.
- Kostka, P. M., Weissmann, M., Buras, R., Mayer, B., and Stiller, O.: Observation Operator for Visible and Near-Infrared Satellite Reflectances, *J. Atmos. Ocean. Tech.*, 31, 1216–1233, <https://doi.org/10.1175/JTECH-D-13-00116.1>, 2014.
- Langenbach, A., Baumgarten, G., Fiedler, J., Lübken, F.-J., von Savigny, C., and Zalach, J.: Year-round stratospheric aerosol backscatter ratios calculated from lidar measurements above northern Norway, *Atmos. Meas. Tech.*, 12, 4065–4076, [https://doi.org/10.5194/amt-12-](https://doi.org/10.5194/amt-12-4065-2019)  
30 4065-2019, 2019.
- Lawson, R. P., Jensen, E., Mitchell, D. L., Baker, B., Mo, Q. X., and Pilson, B.: Microphysical and radiative properties of tropical clouds investigated in TC4 and NAMMA, *J. Geophys. Res.*, 115, D00J08, <https://doi.org/10.1029/2009JD013017>, 2010.
- Li, J., Menzel, W. P., Yang, Z., Frey, R. A., and Ackerman, S. A.: High-Spatial-Resolution Surface and Cloud-Type Classification from MODIS Multispectral Band Measurements, *Journal of Applied Meteorology*, 42, 204–226, [https://doi.org/10.1175/1520-](https://doi.org/10.1175/1520-0450(2003)042<0204:HSRAC>2.0.CO;2)  
35 0450(2003)042<0204:HSRAC>2.0.CO;2, 2003.
- Lindsay, R., Wensnahan, M., Schweiger, A., and Zhang, J.: Evaluation of Seven Different Atmospheric Reanalysis Products in the Arctic, *Journal of Climate*, 27, 2588–2606, <https://doi.org/10.1175/JCLI-D-13-00014.1>, 2014.

- Loewe, K., Ekman, A. M. L., Paukert, M., Sedlar, J., Tjernström, M., and Hoose, C.: Modelling micro- and macrophysical contributors to the dissipation of an Arctic mixed-phase cloud during the Arctic Summer Cloud Ocean Study (ASCOS), *Atmos. Chem. Phys.*, <https://doi.org/10.5194/acp-17-6693-2017>, 2017.
- Lucy, L. B.: An iterative technique for the rectification of observed distributions, *Astron. J.*, 79, 745, <https://doi.org/10.1086/111605>, 1974.
- 5 Luo, Y. L., Xu, K. M., Morrison, H., McFarquhar, G. M., Wang, Z., and Zhang, G.: Multi-layer arctic mixed-phase clouds simulated by a cloud-resolving model: Comparison with ARM observations and sensitivity experiments, *J. Geophys. Res.*, 113, D12 208, <https://doi.org/10.1029/2007JD009563>, 2008.
- Maahn, M., Löhnert, U., Kollias, P., Jackson, R. C., and McFarquhar, G. M.: Developing and Evaluating Ice Cloud Parameterizations for Forward Modeling of Radar Moments Using in situ Aircraft Observations, *J. Atmos. Ocean. Tech.*, 32, 880–903, <https://doi.org/10.1175/JTECH-D-14-00112.1>, 2015.
- 10 Marchand, R. T., Ackermann, T. P., and Moroney, C.: An assessment of Multiangle Imaging Spectroradiometer (MISR) stereoderived cloud top heights and cloud top winds using groundbased radar, lidar, and microwave radiometers, *J. Geophys. Res.*, 112, D06 204, <https://doi.org/10.1029/2006JD007091>, 2007.
- Marshak, A., Platnick, S., Varnai, T., Wen, G. Y., and Cahalan, R. F.: Impact of three-dimensional radiative effects on satellite retrievals of cloud droplet sizes, *J. Geophys. Res.*, 111, <https://doi.org/10.1029/2005JD006686>, 2006.
- 15 Martin, G. M., Johnson, D. W., and Spice, A.: The measurement and parameterization of effective radius of droplets in warm stratocumulus, *J. Atmos. Sci.*, 51, 1823–1842, [https://doi.org/10.1175/1520-0469\(1994\)051<1823:TMAPOE>2.0.CO;2](https://doi.org/10.1175/1520-0469(1994)051<1823:TMAPOE>2.0.CO;2), 1994.
- Mayer, B. and Kylling, A.: Technical note: The *libRadtran* software package for radiative transfer calculations - description and examples of use, *Atmos. Chem. Phys.*, 5, 1855–1877, <https://doi.org/10.5194/acp-5-1855-2005>, 2005.
- 20 McFarquhar, G. M., Zhang, G., Poellot, M. R., Kok, G. L., McCoy, R., Tooman, T., Fridlind, A., and Heymsfield, A. J.: Ice properties of single-layer stratocumulus during the Mixed-Phase Arctic Cloud Experiment: 1. Observations, *J. Geophys. Res.*, 112, D24 201, <https://doi.org/10.1029/2007JD008633>, 2007.
- McGill, M. J., Li, L., Hart, W. D., Heymsfield, G. M., Hlavka, D. L., Racette, P. E., Tian, L., Vaughan, M. A., and Winker, D. M.: Combined lidar-radar remote sensing: Initial results from CRYSTAL-FACE, *J. Geophys. Res.*, 109, D07 203, <https://doi.org/10.1029/2003JD004030>, 25 2004.
- Mech, M., Kliesch, L.-L., Anhäuser, A., Rose, T., Kollias, P., and Crewell, S.: Microwave Radar/radiometer for Arctic Clouds MiRAC: First insights from the ALOUD campaign, *Atmos. Meas. Tech.*, 2019, 1–32, <https://doi.org/10.5194/amt-12-5019-2019>, 2019.
- Mellado, J. P.: Cloud-Top Entrainment in Stratocumulus Clouds, *Annu. Rev. Fluid Mech.*, 49, 145–69, <https://doi.org/10.1146/annurev-fluid-010816-060231>, 2017.
- 30 Miller, S. D., Noh, Y.-J., and Heidinger, A. K.: Liquid-top mixed-phase cloud detection from shortwave-infrared satellite radiometer observations: A physical basis, *J. Geophys. Res.*, 119, 8245–8267, <https://doi.org/10.1002/2013JD021262>, 2014.
- Mioche, G., Jourdan, O., Ceccaldi, M., and Delanoë, J.: Variability of mixed-phase clouds in the Arctic with a focus on the Svalbard region: a study based on spaceborne active remote sensing, *Atmos. Chem. Phys.*, 15, 2445–2461, <https://doi.org/10.5194/acp-15-2445-2015>, 2015.
- Mioche, G., Jourdan, O., Delanoë, J., Gourbeyre, C., Febvre, G., Dupuy, R., Monier, M., Szczap, F., Schwarzenboeck, A., and Gayet, J.-F.: Vertical distribution of microphysical properties of Arctic springtime low-level mixed-phase clouds over the Greenland and Norwegian seas, *Atmos. Chem. Phys.*, 17, 12 845–12 869, <https://doi.org/10.5194/acp-17-12845-2017>, 2017.
- Morrison, H., de Boer, G., Feingold, G., Harrington, J., Shupe, M. D., and Sulia, K.: Resilience of persistent Arctic mixed-phase clouds, *Nat. Geosci.*, 5, 11–17, <https://doi.org/10.1038/NCEO1332>, 2012.

- Nakajima, T. and King, M.: Determination of the optical thickness and effective particle radius of clouds from reflected solar radiation measurements. Part I: Theory, *J. Atmos. Sci.*, 47, 1878–1893, [https://doi.org/10.1175/1520-0469\(1990\)047<1878:DOTOTA>2.0.CO;2](https://doi.org/10.1175/1520-0469(1990)047<1878:DOTOTA>2.0.CO;2), 1990.
- Neggers, R. A. J., Chylik, J., Egerer, U., Griesche, H., Schemann, V., Seifert, P., Siebert, H., and Macke, A.: Local and Remote Controls on Arctic Mixed-Layer Evolution, *J. Adv. Model. Earth Sy.*, 11, 2214–2237, <https://doi.org/10.1029/2019MS001671>, 2019.
- Neuber, R., Schmidt, L. V., Ritter, C., and Mech, M.: Cloud top altitudes observed with airborne lidar during the ALOUD campaign, <https://doi.org/10.1594/PANGAEA.899962>, 2019.
- Nomokonova, T., Ebell, K., Löhnert, U., Maturilli, M., Ritter, C., and O'Connor, E.: Statistics on clouds and their relation to thermodynamic conditions at Ny-Ålesund using ground-based sensor synergy, *Atmos. Chem. Phys.*, 19, 4105–4126, <https://doi.org/10.5194/acp-19-4105-2019>, 2019.
- Pilewskie, P. and Twomey, S.: Discrimination of ice from water in clouds by optical remote sensing, *Atmos. Res.*, 21, 113–122, [https://doi.org/10.1016/0169-8095\(87\)90002-0](https://doi.org/10.1016/0169-8095(87)90002-0), 1987.
- Pithan, F., Svensson, G., Caballero, R., Chechin, D., Cronin, T. W., Ekman, A. M. L., Neggers, R., Shupe, M. D., Solomon, A., Tjernström, M., and Wendisch, M.: Role of air-mass transformations in exchange between the Arctic and mid-latitudes, *Nat. Geosci.*, 11, 805–812, <https://doi.org/10.1038/s41561-018-0234-1>, 2018.
- Platnick, S.: Vertical photon transport in cloud remote sensing problems, *J. Geophys. Res.*, 105, 22 919–22 935, <https://doi.org/10.1029/2000JD900333>, 2000.
- Pu, R.: Hyperspectral remote sensing: Fundamentals and practices, <https://doi.org/10.1201/9781315120607>, 2017.
- Richardson, W. H.: Bayesian-Based Iterative Method of Image Restoration, *J. Opt. Soc. Am.*, 62, 55–59, <https://doi.org/10.1364/JOSA.62.000055>, 1972.
- Riedi, J., Marchant, B., Platnick, S., Baum, B. A., Thieuleux, F., Oudard, C., Parol, F., Nicolas, J. M., and Dubuisson, P.: Cloud thermodynamic phase inferred from merged POLDER and MODIS data, *Atmos Chem Phys*, 10, 11 851–11 865, <https://doi.org/10.5194/acp-10-11851-2010>, 2010.
- Roesler, E. L., Posselt, D. J., and Rood, R. B.: Using large eddy simulations to reveal the size, strength, and phase of updraft and downdraft cores of an Arctic mixed-phase stratocumulus cloud, *J. Geophys. Res. Atmos.*, 122, 4378–4400, <https://doi.org/10.1002/2016JD026055>, 2017.
- Ruiz-Donoso, E., Ehrlich, A., Schäfer, M., Jäkel, E., and Wendisch, M.: Spectral solar cloud top radiance measured by airborne spectral imaging during the ALOUD campaign in 2017, <https://doi.org/10.1594/PANGAEA.902150>, 2019.
- Schäfer, M., Bierwirth, E., Ehrlich, A., Heyner, F., and Wendisch, M.: Retrieval of cirrus optical thickness and assessment of ice crystal shape from ground-based imaging spectrometry, *Atmos. Meas. Tech.*, 6, 1855–1868, <https://doi.org/10.5194/amt-6-1855-2013>, 2013.
- Schäfer, M., Bierwirth, E., Ehrlich, A., Jäkel, E., Werner, F., and Wendisch, M.: Directional, horizontal inhomogeneities of cloud optical thickness fields retrieved from ground-based and airborne spectral imaging, *Atmos. Chem. Phys.*, 17, 2359–2372, <https://doi.org/10.5194/acp-17-2359-2017>, 2017.
- Schäfer, M., Loewe, K., Ehrlich, A., Hoose, C., and Wendisch, M.: Simulated and observed horizontal inhomogeneities of optical thickness of Arctic stratus, *Atmos. Chem. Phys.*, <https://doi.org/10.5194/acp-18-13115-2018>, 2018.
- Schemann, V. and Ebell, K.: Simulation of mixed-phase clouds with the ICON large-eddy model in the complex Arctic environment around Ny-Ålesund, *Atmos. Chem. Phys.*, 20, 475–485, <https://doi.org/10.5194/acp-20-475-2020>, 2020.

- Schnaiter, M. and Järvinen, E.: SID-3 analysis results for 2D scattering patterns during the ACLOUD campaign in 2017, <https://doi.org/10.1594/PANGAEA.900380>, <https://doi.org/10.1594/PANGAEA.900380>, 2019a.
- Schnaiter, M. and Järvinen, E.: SID-3 1Hz size distribution of cloud particles during the ACLOUD campaign in 2017, <https://doi.org/10.1594/PANGAEA.900261>, 2019b.
- 5 Schnaiter, M., Järvinen, E., Vochezer, P., Abdelmonem, A., Wagner, R., Jourdan, O., Mioche, G., Shcherbakov, V. N., Schmitt, C. G., Tricoli, U., Ulanowski, Z., and Heymsfield, A. J.: Cloud chamber experiments on the origin of ice crystal complexity in cirrus clouds, *Atmos. Chem. Phys.*, 16, 5091–5110, <https://doi.org/10.5194/acp-16-5091-2016>, 2016.
- Sedlar, J. and Tjernström, M.: Clouds, warm air, and a climate cooling signal over the summer Arctic, *Geophys. Res. Lett.*, 44, 1095–1103, <https://doi.org/10.1002/2016GL071959>, 2017.
- 10 Seifert, A. and Beheng, K. D.: A two-moment cloud microphysics parameterization for mixed-phase clouds. Part 1: Model description, *Meteorol. Atmos. Phys.*, 92, 45–66, <https://doi.org/10.1007/s00703-005-0112-4>, 2006.
- Serreze, M. C. and Barry, R. G.: Processes and impacts of Arctic amplification: A research synthesis, *Global Planet. Change*, 77, 85–96, <https://doi.org/10.1016/j.gloplacha.2011.03.004>, 2011.
- Shettle, E.: Models of aerosols, clouds, and precipitation for atmospheric propagation studies, *AGARD Conf. Proce.*, -1, 1990.
- 15 Shupe, M. D.: A ground-based multisensor cloud phase classifier, *Geophys. Res. Lett.*, 34, L22 809, 2007.
- Shupe, M. D.: Clouds at Arctic atmospheric observatories. Part II: Thermodynamic phase characteristics, *J. Appl. Meteorol. and Clim.*, 50, 645–661, <https://doi.org/10.1175/2010JAMC2468.1>, 2011.
- Shupe, M. D., Uttal, T., and Matrosov, S. Y.: Arctic cloud microphysics retrievals from surface-based remote sensors at SHEBA, *J. Appl. Meteor.*, 44, 1544–1562, <https://doi.org/10.1175/JAM2297.1>, 2005.
- 20 Shupe, M. D., Matrosov, S. Y., and Uttal, T.: Arctic mixed-phase cloud properties derived from surface-based sensors at SHEBA, *J. Atmos. Sci.*, 63, 697–711, <https://doi.org/10.1175/JAS3659.1>, 2006.
- Shupe, M. D., Kollias, P., Persson, P. O. G., and McFarquhar, G. M.: Vertical motions in Arctic mixed-phase stratiform clouds, *J. Atmos. Sci.*, 65, 1304–1322, <https://doi.org/10.1175/2007JAS2479.1>, 2008.
- Stachlewska, I. S., Neuber, R., Lapmper, A., Ritter, C., and Wehrle, G.: AMALi – the Airborne Mobile Aerosol Lidar for Arctic research, *Atmos. Chem. Phys.*, 10, 2947–2963, <https://doi.org/doi:10.5194/acp-10-2947-2010>, 2010.
- 25 Stammes, K., Tsay, S.-C., Wiscombe, W., and Laszlo, I.: DISORT, a General-Purpose Fortran Program for Discrete-Ordinate-Method Radiative Transfer in Scattering and Emitting Layered Media: Documentation of Methodology, Tech. rep., Dept. of Physics and Engineering Physics, Stevens Institute of Technology, Hoboken, NJ 07030, 2000.
- Stephens, G., Vane, D., Boain, R., Mace, G., Sassen, K., Wang, Z., Illingworth, A., O'Connor, E., Rossow, W., Durden, S., Miller, S., Austin, R., Benedetti, A., Mitrescu, C., and the CloudSat Science Team: The CloudSat mission and the A-train, *Bull. Amer. Meteorol. Soc.*, 83, 1771–1790, <https://doi.org/10.1175/BAMS-83-12-1771>, 2002.
- 30 Tan, I. and Storelvmo, T.: Sensitivity Study on the Influence of Cloud Microphysical Parameters on Mixed-Phase Cloud Thermodynamic Phase Partitioning in CAM5, *J. Atmos. Sci.*, 73, 709–728, <https://doi.org/10.1175/JAS-D-15-0152.1>, 2016.
- Tan, I. and Storelvmo, T.: Evidence of Strong Contributions From Mixed-Phase Clouds to Arctic Climate Change, *Geophysical Research Letters*, 46, 2894–2902, <https://doi.org/10.1029/2018GL081871>, 2019.
- 35 Thompson, D. R., McCubbin, I., Gao, B. C., Green, R. O., Matthews, A. A., Mei, F., Meyer, K. G., Platnick, S., Schmid, B., Tomlinson, J., and Wilcox, E.: Measuring cloud thermodynamic phase with shortwave infrared imaging spectroscopy, *J. Geophys. Res. Atmos.*, 121, 9174–9190, <https://doi.org/10.1002/2016JD024999>, 2016.

- Thompson, D. R., Kahn, B. H., Green, R. O., Chien, S. A., Middleton, E. M., and Tran, D. Q.: Global spectroscopic survey of cloud thermodynamic phase at high spatial resolution, 2005–2015, *Atmos. Meas. Tech.*, 11, 1019–1030, <https://doi.org/10.5194/amt-11-1019-2018>, 2018.
- 5 Tjernström, M., Shupe, M. D., Brooks, I. M., Persson, P. O. G., Prytherch, J., Salisbury, D. J., Sedlar, J., Achtert, P., Brooks, B. J., Johnston, P. E., Sotiropoulou, G., and Wolfe, D.: Warm-air advection, air mass transformation and fog causes rapid ice melt, *Geophys. Res. Lett.*, 42, 5594–5602, <https://doi.org/10.1002/2015GL064373>, 2015.
- Vochezer, P., Järvinen, E., Wagner, R., Kupiszewski, P., Leisner, T., and Schnaiter, M.: In situ characterization of mixed phase clouds using the Small Ice Detector and the Particle Phase Discriminator, *Atmos. Meas. Tech.*, 9, 159–177, <https://doi.org/10.5194/amt-9-159-2016>, 2016.
- 10 Wang, S., Zheng, X., and Jiang, Q.: Strong sheared stratocumulus convection: An observationally based large-eddy simulation study, *Atmos. Chem. Phys.*, 12, 5223–5235, 2012.
- Wendisch, M., Müller, D., Schell, D., and Heintzenberg, J.: An airborne spectral albedometer with active horizontal stabilization, *J. Atmos. Oceanic Technol.*, 18, 1856–1866, [https://doi.org/10.1175/1520-0426\(2001\)018<1856:AASAWA>2.0.CO;2](https://doi.org/10.1175/1520-0426(2001)018<1856:AASAWA>2.0.CO;2), 2001.
- Wendisch, M., Brückner, M., Burrows, J. P., Crewell, S., Dethloff, K., Ebell, K., Lüpkes, C., Macke, A., Notholt, J., Quaas, J., Rinke, A., and  
 15 Tegen, I.: Understanding causes and effects of rapid warming in the Arctic, *Eos*, 98, <https://doi.org/10.1029/2017EO064803>, 2017.
- Wendisch, M., Macke, A., Ehrlich, A., Lüpkes, C., Mech, M., Chechin, D., Dethloff, K., Velasco, C. B., Bozem, H., Brückner, M., Clemen, H.-C., Crewell, S., Donth, T., Dupuy, R., Ebell, K., Egerer, U., Engelmann, R., Engler, C., Eppers, O., Gehrmann, M., Gong, X., Gottschalk, M., Gourbeyre, C., Griesche, H., Hartmann, J., Hartmann, M., Heinold, B., Herber, A., Herrmann, H., Heygster, G., Hoor, P., Jafariserajehlou, S., Jäkel, E., Järvinen, E., Jourdan, O., Kästner, U., Kecorius, S., Knudsen, E. M., Köllner, F., Kretzschmar, J., Lelli, L.,  
 20 Leroy, D., Maturilli, M., Mei, L., Mertes, S., Mioche, G., Neuber, R., Nicolaus, M., Nomokonova, T., Notholt, J., Palm, M., van Pinxteren, M., Quaas, J., Richter, P., Ruiz-Donoso, E., Schäfer, M., Schmieder, K., Schnaiter, M., Schneider, J., Schwarzenböck, A., Seifert, P., Shupe, M. D., Siebert, H., Spreen, G., Stapf, J., Stratmann, F., Vogl, T., Welti, A., Wex, H., Wiedensohler, A., Zanatta, M., and Zeppenfeld, S.: The Arctic Cloud Puzzle: Using ALOUD/PASCAL Multiplatform Observations to Unravel the Role of Clouds and Aerosol Particles in Arctic Amplification, *Bull. Amer. Meteor. Soc.*, 100, 841–871, <https://doi.org/10.1175/BAMS-D-18-0072.1>, 2019.
- 25 Werner, F., Siebert, H., Pilewskie, P., Schmeissner, T., Shaw, R. A., and Wendisch, M.: New airborne retrieval approach for trade wind cumulus properties under overlying cirrus, *J. Geophys. Res. Atmos.*, 118, 3634–3649, <https://doi.org/10.1002/jgrd.50334>, 2013.
- Werner, F., Ditas, F., Siebert, H., Simmel, M., Wehner, B., Pilewskie, P., Schmeissner, T., Shaw, R. A., Hartmann, S., Wex, H., Roberts, G. C., and Wendisch, M.: Twomey effect observed from collocated microphysical and remote sensing measurements over shallow cumulus, *J. Geophys. Res.*, 119, 1534–1545, <https://doi.org/10.1002/2013JD020131>, 2014.
- 30 Wesche, C., Steinhage, D., and Nixdorf, U.: Polar aircraft Polar5 and Polar6 operated by the Alfred Wegener Institute, *J. Large-Scale Res. Facilities*, 2, A87, <https://doi.org/10.17815/jlsrf-2-153>, 2016.
- Woods, C., Caballero, R., and Svensson, G.: Large-scale circulation associated with moisture intrusions into the Arctic during winter, *Geophys. Res. Lett.*, 40, 4717–4721, <https://doi.org/10.1002/grl.50912>, 2013.
- Yang, P., Liou, K. N., Wyser, K., and Mitchell, D.: Parameterization of the scattering and absorption properties of individual ice crystals, *J. Geophys. Res.*, 105, 4,699–4,718, <https://doi.org/10.1029/1999JD900755>, 2000.
- 35 Zhou, L., Liu, Q., Liu, D., Xie, L., Qi, L., and Liu, X.: Validation of MODIS liquid water path for oceanic nonraining warm clouds: Implications on the vertical profile of cloud water content, *J. Geophys. Res. Atmos.*, 121, 4855–4876, <https://doi.org/10.1002/2015JD024499>, 2016.

Zinner, T. and Mayer, B.: Remote sensing of stratocumulus clouds: Uncertainties and biases due to inhomogeneity, *Journal of Geophysical Research: Atmospheres*, 111, <https://doi.org/10.1029/2005JD006955>, 2006.

Zinner, T., Mayer, B., and Schröder, M.: Determination of 3D cloud structures from high resolution radiance data, *J. Geophys. Res.*, 111, doi:10.1029/2005JD006062, 2006.